Elasto-capillary fluid-structure interaction with compound droplets

Sthavishtha R. Bhopalam[a], Jesus Bueno[b], Hector Gomez[a,*]

[a]*School of Mechanical Engineering, Purdue University, West Lafayette, IN 47907, USA.*
[b]*Midge Medical GmbH, Colditzstraße 34/36, 16A, Berlin 12099, Germany.*

Abstract

Computational modeling of elasto-capillarity, i.e., a fluid-structure interaction phenomenon where the solid deformation is driven by capillary forces at fluid-fluid interfaces has recently emerged as an important problem in computational mechanics. However, the high-fidelity simulation of elasto-capillary problems involving three immiscible fluids has remained unexplored. Here, we present a mathematical model and an algorithm to simulate elasto-capillary problems involving compound droplets. Such problems are of pivotal importance in pharmaceutical, biological and food industrial applications. We adopt a phase-field model described by the ternary Navier-Stokes-Cahn-Hilliard equations for the three immiscible fluids and a neo-Hookean model for the solid. We define a fluid-solid surface energy function, which determines the fluid-solid wettability and the tractions transmitted to the solid at the fluid-solid interface. We adopt a boundary-fitted approach for our fluid-structure interaction formulation and Isogeometric Analysis for the spatial discretization. To demonstrate the effectiveness of our computational model and algorithm, we perform elasto-capillary simulations involving various types of compound droplets.

Keywords: Elasto-capillarity, Fluid-structure interaction (FSI), ternary Navier-Stokes-Cahn-Hilliard (tNSCH), Isogeometric analysis (IGA), Compound droplets.

1. Introduction

Fluid-structure interaction (FSI) plays an important role in many scientific and engineering applications [1–5], some of which involve multiphase fluids; see [6–8] for detailed reviews. Traditional numerical methods for solving classical FSI involving multiphase fluids [9–12] have been largely limited to large-scale problems, where the effect of surface tension on solid deformation is negligible. However, in FSI problems at micro- and nano-scales, forces due to surface tension play a crucial role in deforming the solid. The deformation of an elastic solid by capillary forces at the fluid-fluid interfaces is termed elasto-capillarity or soft wetting. Elasto-capillarity is important in many applications, such as, ink-jet printing [13], microfabrication [14] and biophysics [15]. Many intriguing experiments involving elasto-capillarity have been recently reported, such as, spontaneous migration of droplets on deformable surfaces [16–19], self-wrapping of droplets in contact with elastic membranes (termed as *capillary-origami*) [4] and wrinkling patterns arising upon the placement of droplets on thin bendable sheets [20]. However, this exciting experimental research has not been accompanied by a similar amount of computational research due to the unique challenges presented by elasto-capillary simulations.

Modeling and simulation of FSI problems with multiphase flows and capillary forces have remained an outstanding problem until recently; see [21] and [17, 22–28]. Most previous studies on

*Corresponding author email: hectorgomez@purdue.edu

elasto-capillary FSI have used phase-field methods. The key idea in phase-field methods is to use an order parameter, also called phase-field, to identify distinct fluid phases or distinct fluid components. The phase-field is defined on the entire computational domain and evolves in time governed by partial-differential equations (PDEs) that can be derived from continuum mechanics or asymptotic variational problems [29]. The popularity of phase-field methods in solving elasto-capillary FSI problems is due to multiple reasons. Firstly, phase field methods avoid the contact-line stress singularities [30]. Additionally, phase field methods can describe the dynamic wetting behavior [31, 32], moving contact lines, can enforce thermodynamical consistency of the models [22] and can easily include the solid-fluid surface tension effects in the fluid-solid interface conditions [22, 30, 33].

Existing elasto-capillary simulations have focused on fluid models that involve a single-component fluid that undergoes liquid-vapor phase transformations [17, 24] or two immiscible components that do not undergo phase transformations [22, 23, 25, 26, 28, 34], using, respectively, the Navier-Stokes-Korteweg (NSK) and the Navier-Stokes-Cahn-Hilliard (NSCH) equations. However, despite its importance, the simulation of elasto-capillary problems involving three immiscible fluid components remains unexplored. A computational method to simulate these problems would enable the study of elasto-capillary problems involving compound droplets. The applications of compound droplets are diverse, ranging from pharmaceutics, biology, atmospheric chemistry to food industry [35, 36]. This paper proposes a mathematical model and an algorithm for the simulation of elasto-capillarity problems involving compound droplets. In our model, compound droplets are comprised of two immiscible fluids (e.g., water and oil) which are immersed in a third ambient fluid (e.g., air). The phase-field model for three-component flow of immiscible fluids is given by the ternary Navier-Stokes-Cahn-Hilliard equations (tNSCH). Although the tNSCH equations have been very successful in describing the dynamics of three immiscible fluids, there are still open theoretical questions about the behavior of the equations in the so-called total spreading regime [37]. Notably, the tNSCH have not been used in the context of FSI. A critical aspect of our model of elasto-capillary FSI of compound droplets is the definition of the surface energy function at the fluid-solid interface because it regulates the wettability of the solid with respect to the three fluids and determines the tractions that are transmitted to the solid at the fluid-solid interface. We propose a new approach to derive this surface energy function using consistency conditions compatible with those introduced in [37] for the governing equations in the bulk. We adopt a neo-Hookean model with a dilatational penalty to describe the dynamics of the solid. Our FSI formulation is based on a boundary-fitted algorithm in which the fluid-solid interface is defined explicitly [38]. This approach permits an accurate computation of the capillary forces at the interface, which is important in elasto-capillary simulations. In our computations, the fluid domain does not undergo topological changes, and we simply have to use a mesh-update algorithm, which facilitates the implementation of the boundary-fitted method. The spatial discretization is based on Isogeometric Analysis (IGA) [39, 40], a generalization of finite elements that allows to use basis functions with controllable inter-element continuity on mapped geometries. The time discretization is performed using the generalized-α method. To solve the linear algebra problem, we adopt a quasi-direct solution strategy [38] in which the fluid and solid equations are solved monolithically, while the mesh update equations are solved separately, using the data from the fluid-solid solver as input. The performance of the model and algorithm are illustrated with a validation example and several elasto-capillary simulations of compound droplets. The results show the complexity of elastocapillarity problems with compound droplets and highlight the importance of high-fidelity models.

The outline of the paper is as follows: In Sec. 2, we present the governing equations of the fluid mechanics and solid mechanics problems. We also present the initial conditions, boundary conditions and fluid-solid interface conditions. In Sec. 3, we describe the variational formulation of the fluid-structure interaction problem in the continuous and semi-discrete forms. In the same

Section, we additionally detail our time discretization and solution strategy for solving the semi-discrete form of the equations. We present a series of numerical examples in Sec. 4 to demonstrate the capability of our model and algorithm. Lastly, we summarize our conclusions in Sec. 5.

2. Governing equations

2.1. Kinematics

Let $\Omega_{\widehat{\boldsymbol{x}}} \in \mathbb{R}^d$, $\Omega_t \in \mathbb{R}^d$ and $\Omega_{\boldsymbol{X}} \in \mathbb{R}^d$ denote, respectively, the reference, spatial and material domains occupied by a continuum body, where d is the number of spatial dimensions. These domains are assumed to be open sets. The spatial and material domains are also termed as the Eulerian and Lagrangian domains, respectively. Let $\Omega_{\widehat{\boldsymbol{x}}}$ be fixed in time and its points be parameterized by the reference coordinates $\widehat{\boldsymbol{x}}$. We define the function $\widehat{\boldsymbol{\phi}}$ which maps the referential to spatial domain at time t as

$$\begin{aligned} \widehat{\boldsymbol{\phi}}(\cdot, t) : \Omega_{\widehat{\boldsymbol{x}}} &\longmapsto \Omega_t = \widehat{\boldsymbol{\phi}}(\Omega_{\widehat{\boldsymbol{x}}}, t), \ \forall t \geq 0, \\ \widehat{\boldsymbol{x}} &\longmapsto \boldsymbol{x} = \widehat{\boldsymbol{\phi}}(\widehat{\boldsymbol{x}}, t), \ \forall \widehat{\boldsymbol{x}} \in \Omega_{\widehat{\boldsymbol{x}}}, \end{aligned} \tag{1}$$

where $\boldsymbol{x}$ denotes the coordinates of the spatial domain. With this mapping, the referential displacement and referential velocity can be defined as $\widehat{\boldsymbol{u}}(\widehat{\boldsymbol{x}}, t) := \widehat{\boldsymbol{\phi}}(\widehat{\boldsymbol{x}}, t) - \widehat{\boldsymbol{x}}$ and $\widehat{\boldsymbol{v}} := \partial_t \widehat{\boldsymbol{\phi}} = \partial_t \widehat{\boldsymbol{u}}$, respectively, where the operator ∂_t denotes partial time differentiation. Analogously, we define $\boldsymbol{\phi}$ which maps the material to spatial domain at time t as

$$\begin{aligned} \boldsymbol{\phi}(\cdot, t) : \Omega_{\boldsymbol{X}} &\longmapsto \Omega_t = \boldsymbol{\phi}(\Omega_{\boldsymbol{X}}, t), \ \forall t \geq 0, \\ \boldsymbol{X} &\longmapsto \boldsymbol{x} = \boldsymbol{\phi}(\boldsymbol{X}, t), \ \forall \boldsymbol{X} \in \Omega_{\boldsymbol{X}}, \end{aligned} \tag{2}$$

where $\boldsymbol{X}$ denotes the location of a material particle. The material displacement and material velocity are defined as $\boldsymbol{u}(\boldsymbol{X}, t) := \boldsymbol{\phi}(\boldsymbol{X}, t) - \boldsymbol{X}$ and $\boldsymbol{v} := \partial_t \boldsymbol{\phi} = \partial_t \boldsymbol{u}$, respectively. The deformation gradient is defined as, $\boldsymbol{F} := \frac{\partial \boldsymbol{\phi}}{\partial \boldsymbol{X}}$ and the Jacobian determinant is defined as $J := \det(\boldsymbol{F})$. It follows from the definitions above that the Eulerian velocity is $\boldsymbol{v} \circ \boldsymbol{\phi}^{-1}$. Although the functions $\boldsymbol{v}$ and $\boldsymbol{v} \circ \boldsymbol{\phi}^{-1}$ are different, they represent the same physical quantity and we will use the same symbol for both henceforth. To avoid ambiguity in the definition of the derivatives, we will use subscripts. For example, subscript $\widehat{\boldsymbol{x}}$ in $\partial_t \boldsymbol{v}|_{\widehat{\boldsymbol{x}}}$ indicates that the time derivative has been computed by holding $\widehat{\boldsymbol{x}}$ fixed. When no subscript is specified, we assume the time derivative to be taken by holding $\boldsymbol{x}$ fixed. In the context of spatial derivatives, for example, subscript $\widehat{\boldsymbol{x}}$ in $\nabla_{\widehat{\boldsymbol{x}}} \widehat{\boldsymbol{u}}$ indicates that the spatial derivative has been computed with respect to the reference coordinates $\widehat{\boldsymbol{x}}$. When no subscript is specified, we assume the spatial derivative to be taken with respect to the spatial coordinates $\boldsymbol{x}$.

We will be focusing on a FSI problem. Thus, the spatial domain can be decomposed as $\Omega_t = \Omega_t^f \cup \Omega_t^s$ where Ω_t^f and Ω_t^s are open sets that identify the current configuration of the fluid and solid, respectively and $\Omega_t^f \cap \Omega_t^s = \emptyset$; see Fig. 1a. A similar decomposition applies to the material and reference domains. In our FSI problem, we consider the material and reference domains to be the same. Henceforth, we will denote Ω_0 as the referential or material domain of the combined fluid and solid. We will also denote Γ_t^f as the fluid boundary without the fluid-solid interface in the spatial domain and Γ_t^{sf} as the fluid-solid interface in the spatial domain.

2.2. Governing equations of fluid mechanics

The dynamics of the three immiscible fluids is described by the ternary Navier-Stokes-Cahn-Hilliard (tNSCH) equations. We assume that the three fluids share the same density and dynamic

viscosity, which are both constant [37, 41]. We describe the fluids' motion by a single velocity field. The Ginzburg-Landau free energy per unit volume of the fluid mixture is [37, 41]

$$\psi^f = \frac{12}{\epsilon}F(c_1, c_2, c_3) + \frac{3}{8}\epsilon\Sigma_1|\nabla c_1|^2 + \frac{3}{8}\epsilon\Sigma_2|\nabla c_2|^2 + \frac{3}{8}\epsilon\Sigma_3|\nabla c_3|^2, \tag{3}$$

where ϵ is the diffuse interface length scale, $(c_1, c_2, c_3) \in [0, 1]^3$ are the phase fields denoting the volume fractions of the respective fluid, Σ_1, Σ_2 and Σ_3 are the spreading coefficients and F is the bulk free energy. The expression for the bulk free energy is

$$F(c_1, c_2, c_3) = \frac{\Sigma_1}{2}c_1^2(1 - c_1)^2 + \frac{\Sigma_2}{2}c_2^2(1 - c_2)^2 + \frac{\Sigma_3}{2}c_3^2(1 - c_3)^2. \tag{4}$$

The last three terms in Eq. (3) represent the interfacial free energy. The spreading coefficients are computed from the surface tensions as

$$\begin{aligned}\Sigma_1 &= \gamma_{12} + \gamma_{13} - \gamma_{23},\\ \Sigma_2 &= \gamma_{23} + \gamma_{12} - \gamma_{13},\\ \Sigma_3 &= \gamma_{13} + \gamma_{23} - \gamma_{12},\end{aligned} \tag{5}$$

where γ_{ij} denotes the surface tension at the interface between fluids i and j. Because the phase fields represent volume fractions, admissible solutions belong to the hyperplane

$$\mathcal{G} = \{\boldsymbol{c} = (c_1, c_2, c_3) \in [0, 1]^3,\ c_1 + c_2 + c_3 = 1\}. \tag{6}$$

The constraint $\boldsymbol{c} \in \mathcal{G}$ will be imposed using a Lagrange multiplier. Therefore, we will only solve equations for c_1 and c_2, and we will obtain c_3 from the constraint $c_1 + c_2 + c_3 = 1$. The governing equations in the Eulerian frame are given by

$$\nabla \cdot \boldsymbol{v} = 0, \tag{7a}$$

$$\rho\, \partial_t \boldsymbol{v}|_{\boldsymbol{X}} = \nabla \cdot \boldsymbol{\sigma}^f + \rho \boldsymbol{f}, \tag{7b}$$

$$\partial_t c_i|_{\boldsymbol{X}} = \nabla \cdot \left(\frac{M_0}{\Sigma_i}\nabla\mu_i\right);\ i = 1, 2, \tag{7c}$$

$$\mu_i = -\frac{3}{4}\epsilon\Sigma_i\Delta c_i + \frac{12}{\epsilon}\Sigma_i c_i(1 - c_i)(1 - 2c_i) - \frac{12\delta}{\epsilon}c_1c_2(1 - c_1 - c_2);\ i = 1, 2, \tag{7d}$$

where $\boldsymbol{v}$ is the fluid velocity, ρ is the fluid density, $\boldsymbol{\sigma}^f$ is the fluid stress tensor, $\boldsymbol{f}$ is the body force per unit mass, $M_0 > 0$ is the mobility coefficient associated with the diffusive flux of the fluid mixture, μ_i is the chemical potential associated with the diffusive flux of fluid i and $\delta = 6\left(\frac{1}{\Sigma_1} + \frac{1}{\Sigma_2} + \frac{1}{\Sigma_3}\right)^{-1}$. The last term in Eq. (7d) is the Lagrange multiplier used to enforce the constraint $c_1 + c_2 + c_3 = 1$. The fluid stress tensor is defined as

$$\begin{aligned}\boldsymbol{\sigma}^f = &-p\boldsymbol{I} + 2\eta\nabla^s\boldsymbol{v} - \frac{3}{4}\epsilon\left(\Sigma_1 + \Sigma_3\right)\nabla c_1 \otimes \nabla c_1 - \frac{3}{4}\epsilon\left(\Sigma_2 + \Sigma_3\right)\nabla c_2 \otimes \nabla c_2\\ &- \frac{3}{4}\epsilon\Sigma_3\left(\nabla c_1 \otimes \nabla c_2 + \nabla c_2 \otimes \nabla c_1\right).\end{aligned} \tag{8}$$

where p is the pressure, η is the dynamic viscosity of the fluid and ∇^s denotes the symmetrization of the spatial gradient operator.

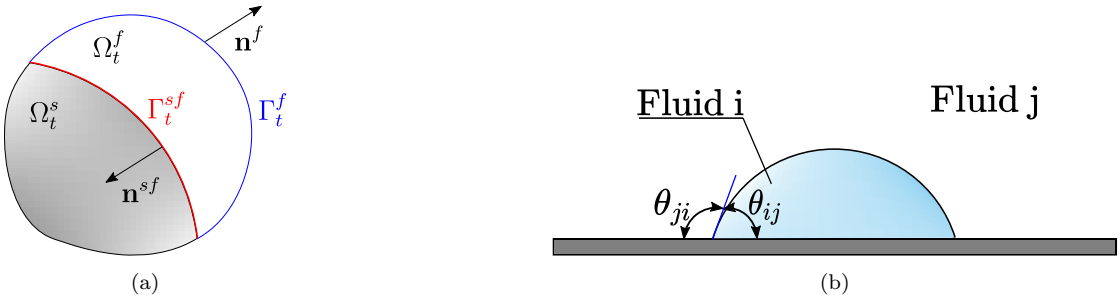

Figure 1: (Color figure online) a) Schematic showing the spatial domain of the fluid (Ω_t^f) and solid (Ω_t^s). We also show the direction of the unit normal vector $\boldsymbol{n}^{sf}$ at the fluid-solid interface in the spatial domain (Γ_t^{sf}) and the unit normal $\boldsymbol{n}^f$ at the fluid boundary without the fluid-solid interface in the spatial domain (Γ_t^f). b) Illustration of the static contact angles θ_{ij} and θ_{ji} formed by the fluid-fluid interface with the solid.

Remark 2.1. The governing equations given in Eq. (7) are equivalent to the equations from [37, 41]. If we call $\widetilde{p}$ the pressure used in [37, 41], then our pressure field in Eq. (8) is defined as $p = \widetilde{p} - \psi^f$. We derive Eq. (7) from [37, 41] to express $\boldsymbol{\sigma}^f$ in a conservative form using the constraint $c_1 + c_2 + c_3 = 1$, Eqs. (3)–(4) and the relation

$$\mu_3 = -\Sigma_3 \left(\frac{\mu_1}{\Sigma_1} + \frac{\mu_2}{\Sigma_2} \right), \tag{9}$$

which follows from Eq. (7d) and the constraint $c_1 + c_2 + c_3 = 1$.

From Eq. (5), two cases of spreading coefficients are possible [42]: total spreading, where at least one of $\Sigma_i \leq 0$, and partial spreading, where all $\Sigma_i > 0$. We restrict our system to the latter case. Our system additionally satisfies $\Sigma_i > \frac{\delta}{4} > 0 \ \forall i = 1, 2, 3$ to ensure the positivity of ψ^f; see [37, 41] for the mathematical details and proofs. Additionally, Boyer and Lapuerta [37] proposed two consistency conditions $\mathcal{P}1$ and $\mathcal{P}2$ for the model given by Eqs. (3)–(7). Condition $\mathcal{P}1$ is satisfied if and only if the free energy per unit volume in the three-fluid mixture equals the free energy per unit volume in the two-fluid mixture when one fluid is absent. Condition $\mathcal{P}2$ indicates that if $c_i = 0$ at $t = 0$, then $c_i = 0 \ \forall \ t \geq 0 \ \forall i = 1, 2, 3$.

2.2.1. Initial and boundary conditions for the fluid mechanics equations

For the fluid mechanics equations presented in Eq. (7), we furnish suitable initial and boundary conditions. We provide initial conditions by specifying the phase fields and fluid velocity at the initial time. In our FSI problem, the boundary of the fluid domain is $\Gamma_t^f \cup \Gamma_t^{sf}$. In our problem of interest, Γ_t^f is the external boundary of the computational domain and is placed sufficiently far away from the region of interest. On Γ_t^f, we impose zero normal velocity, zero tangential traction, zero diffusive flux and neutral wettability condition, i.e.,

$$\boldsymbol{n}^f \cdot \boldsymbol{v} = 0 \qquad \text{on } \Gamma_t^f, \tag{10}$$

$$\boldsymbol{t}_e \cdot \boldsymbol{\sigma}^f \boldsymbol{n}^f = 0 \qquad \text{for } e = 1, .., d-1 \text{ on } \Gamma_t^f, \tag{11}$$

$$\boldsymbol{n}^f \cdot \nabla \mu_i = 0 \qquad \text{for } i = 1, 2 \text{ on } \Gamma_t^f, \tag{12}$$

$$\boldsymbol{n}^f \cdot \nabla c_i = 0 \qquad \text{for } i = 1, 2 \text{ on } \Gamma_t^f, \tag{13}$$

where $\boldsymbol{n}^f$ is the unit outward normal vector at Γ_t^f and the $\boldsymbol{t}_e$'s constitute an orthonormal basis of $\mathbb{R}^{d-1}$ that is orthogonal to $\boldsymbol{n}^f$.

On Γ_t^{sf}, we will impose coupling conditions pertaining to the fluid-solid interaction. These are of a different nature and will be described in Sec. 2.4. However, Γ_t^{sf} is an external boundary for the

phase fields (the phase fields are not defined in the solid), and thus we need to equate the unknowns or their derivatives to given data. The first boundary condition for the phase fields that we will impose on Γ_t^{sf} is

$$\boldsymbol{n}^{sf} \cdot \nabla \mu_i = 0 \text{ for } i = 1, 2 \text{ on } \Gamma_t^{sf}, \tag{14}$$

where $\boldsymbol{n}^{sf}$ is the unit normal vector at Γ_t^{sf} pointing in the direction from fluid to solid; see Fig. 1a. Eq. (14) indicates that there is no diffusive flux across the fluid-solid interface. The second boundary condition for the phase fields on Γ_t^{sf} defines the wettability of the three-fluid mixture and the solid. However, the derivation of such wetting boundary conditions is difficult due to three challenges. Firstly, the boundary conditions must allow the motion of fluid-fluid interfaces at the wetting boundary. Secondly, the wetting boundary conditions must satisfy consistency conditions compatible with $\mathcal{P}1$, $\mathcal{P}2$ and $\boldsymbol{c} \in \mathcal{G}$. We found that using boundary conditions that satisfy these conditions is critical for elasto-capillary simulations involving compound droplets. The reason is that these conditions define the fluid-solid wettability, but more importantly determine the traction forces transmitted to the solid. Finally, the wetting boundary conditions must be compatible with the equilibrium in Ω_t^f. Existing wetting boundary condition models in three-fluid mixtures [43–45] have tried to resolve some of these challenges. For our elasto-capillary simulations, the first challenge is automatically addressed by the use of a diffuse interface. To address the second challenge, we derive wetting boundary conditions that satisfy $\mathcal{P}1$, the constraint $\boldsymbol{c} \in \mathcal{G}$ and that are compatible with $\mathcal{P}2$. To make our boundary conditions compatible with $\mathcal{P}2$, we impose that if $c_i = 0$ on Γ_t^{sf} at $t = 0$, then $\boldsymbol{n}^{sf} \cdot \nabla c_i = 0 \ \forall t \geq 0 \ \forall i = 1, 2, 3$ on Γ_t^{sf}. We address the third challenge by minimizing the fluid-solid interfacial energy of the fluid mixture with respect to $\boldsymbol{c}$.

For appropriate imposition of the wetting boundary conditions at Γ_t^{sf}, we firstly define the free energy of the fluid mixture including the contribution from the wetting boundary as

$$\Psi^f = \int_{\Omega_t^f} \psi^f d\Omega_t^f + \int_{\Gamma_t^{sf}} \gamma_{sf} d\Gamma_t, \tag{15}$$

where γ_{sf} is the surface energy density at Γ_t^{sf}. We now derive the wetting boundary conditions by taking the functional derivative of Ψ^f with respect to c_i using calculus of variations, collecting the boundary terms upon subsequent integration by parts and setting them to zero. This procedure ensures that our boundary conditions will not be incompatible with equilibrium in the interior of the domain and leads to

$$\frac{3}{4}\epsilon \Sigma_i \boldsymbol{n}^{sf} \cdot \nabla c_i + \frac{\partial \gamma_{sf}}{\partial c_i} = 0, \ i = 1, 2, 3 \text{ on } \Gamma_t^{sf}, \tag{16}$$

We neglect the Shuttleworth effect [46], allowing us to interpret γ_{sf} as a function of c_1, c_2 and c_3 alone [22, 30, 33]. We define γ_{sf} as,

$$\gamma_{sf}(c_1, c_2, c_3) = R(c_1, c_2, c_3) + Q(c_1, c_2, c_3), \tag{17}$$

where

$$R(c_1, c_2, c_3) = \gamma_{1s}(3c_1^2 - 2c_1^3) + \gamma_{2s}(3c_2^2 - 2c_2^3) + \gamma_{3s}(3c_3^2 - 2c_3^3). \tag{18}$$

In Eq. (18), γ_{is} denotes the surface tension at the interface between the solid and fluid i. Note that γ_{1s}, γ_{2s} and γ_{3s} are related to each other by the Young's relation given as,

$$\cos\theta_{ij} = \frac{\gamma_{js} - \gamma_{is}}{\gamma_{ij}} \ \ i, j = 1, 2, 3, \ i \neq j, \tag{19}$$

where θ_{ij} is the static contact angle at equilibrium between the solid and the interface formed between fluids i and j; see Fig. 1b. The particular choice of R in Eq. (18) is justified as it is a smoothly varying function, which equals γ_{1s}, γ_{2s} and γ_{3s} when (c_1, c_2, c_3) equals $(1,0,0)$, $(0,1,0)$ and $(0,0,1)$ respectively. Additionally, R simplifies to an expression of the solid-fluid surface tension in the case of two-fluid mixture (see [22, 33] for the appropriate expression) when one among c_1, c_2 or c_3 equals 0, i.e., R satisfies $\mathcal{P}1$. We will determine the function Q by imposing the above-described consistency conditions. Q satisfies $\mathcal{P}1$ if and only if

$$Q(0, c, 1-c) = Q(c, 0, 1-c) = Q(c, 1-c, 0) = 0 \ \forall c \in \mathbb{R}. \tag{20}$$

For Eq. (20) to hold valid, we deduce that there exist two smooth functions G and H such that

$$Q(c_1, c_2, c_3) = c_1 c_2 c_3 G(c_1, c_2, c_3) + (c_1 + c_2 + c_3 - 1) H(c_1, c_2, c_3) \tag{21}$$

from [37, Lemma 3.4]. Here, H is a Lagrange multiplier enforcing the constraint $\boldsymbol{c} \in \mathcal{G}$. Substitution of Eqs. (17), (18) and (21) in Eq. (16) gives us

$$\frac{3}{4}\epsilon \Sigma_i \boldsymbol{n}^{sf} \cdot \nabla c_i + \frac{\partial R}{\partial c_i} + \frac{\partial \left(c_1 c_2 c_3 G\right)}{\partial c_i} + H = 0, \ \forall i = 1,2,3 \text{ on } \Gamma_t^{sf}. \tag{22}$$

To enforce $c_1 + c_2 + c_3 = 1$, we divide Eq. (22) by Σ_i and sum it up for all $i \in \{1,2,3\}$, yielding us the expression of H as

$$H = -\frac{\delta}{6}\left(\frac{1}{\Sigma_1}\left(\frac{\partial R}{\partial c_1} + \frac{\partial \left(c_1 c_2 c_3 G\right)}{\partial c_1}\right) + \frac{1}{\Sigma_2}\left(\frac{\partial R}{\partial c_2} + \frac{\partial \left(c_1 c_2 c_3 G\right)}{\partial c_2}\right) + \frac{1}{\Sigma_3}\left(\frac{\partial R}{\partial c_3} + \frac{\partial \left(c_1 c_2 c_3 G\right)}{\partial c_3}\right)\right). \tag{23}$$

Enforcing that if $c_i = 0$ at $t = 0$, then $\boldsymbol{n}^{sf} \cdot \nabla c_i = 0 \ \forall t > 0$ on Eq. (22) implies that

$$\left(\frac{\partial R}{\partial c_i} + c_j c_k G + c_1 c_2 c_3 \frac{\partial G}{\partial c_i} + H\right)\Bigg|_{c_i = 0, c_k = 1 - c_j} = 0, \ i,j,k = 1,2,3, \ \{j,k\} \neq i \text{ and } j \neq k. \tag{24}$$

Eq. (24) is satisfied by triples (c_1, c_2, c_3) of the form $(c, 1-c, 0)$, $(c, 0, 1-c)$ and $(0, c, 1-c)$ $\forall c \in [0,1]$. Substituting Eqs. (18) and (23) in Eq. (24) and performing multiple algebraic manipulations, we get the following conditions on G:

$$\begin{aligned} G(c, 1-c, 0) &= 6\left(\frac{\gamma_{1s}\Sigma_2 + \gamma_{2s}\Sigma_1}{\Sigma_1 + \Sigma_2}\right) \\ G(c, 0, 1-c) &= 6\left(\frac{\gamma_{1s}\Sigma_3 + \gamma_{3s}\Sigma_1}{\Sigma_1 + \Sigma_3}\right) \\ G(0, c, 1-c) &= 6\left(\frac{\gamma_{2s}\Sigma_3 + \gamma_{3s}\Sigma_2}{\Sigma_2 + \Sigma_3}\right). \end{aligned} \tag{25}$$

To satisfy Eq. (25), we propose G to be of the form

$$\begin{aligned} G(c_1, c_2, c_3) = 3\left(\frac{\gamma_{1s}\Sigma_2 + \gamma_{2s}\Sigma_1}{\gamma_{12}}\right) g_{12}(c_1, c_2, c_3) + 3\left(\frac{\gamma_{2s}\Sigma_3 + \gamma_{3s}\Sigma_2}{\gamma_{23}}\right) g_{23}(c_1, c_2, c_3) \\ + 3\left(\frac{\gamma_{1s}\Sigma_3 + \gamma_{3s}\Sigma_1}{\gamma_{13}}\right) g_{13}(c_1, c_2, c_3), \end{aligned} \tag{26}$$

where we have used Eq. (5) and we have introduced the functions g_{ij} with $i < j$ which satisfy

$$g_{ij}(c_1, c_2, c_3) = \begin{cases} 1 & \text{for } c_i + c_j = 1 \text{ and } 0 < c_i < 1, 0 < c_j < 1, \\ 0 & \text{for } c_i = 0 \ \text{ or } \ c_j = 0, \\ > 0 & \text{for } 0 < c_k < 1, \ k \neq \{i,j\} \text{ and, } \{c_i \neq 0 \text{ or } c_j \neq 0\}. \end{cases} \tag{27}$$

We propose the following rational functions which satisfy Eq. (27),

$$g_{ij}(c_1, c_2, c_3) = \frac{c_i c_j}{(1 - c_i)(1 - c_j)}, \quad i, j = 1, 2, 3. \tag{28}$$

Remark 2.2. The functions g_{ij} satisfying the conditions in Eq. (27) are non-unique. We numerically experimented with exponential, rational (Eq. (28)) or rational power functions satisfying Eq. (27) for the case of three immiscible fluids on a rigid solid. We observed no appreciable difference in our results and hence adopted the rational functions given by Eq. (28) for our computations.

Substituting Eqs. (17), (18), (21), (26) and (28) in Eq. (16) we obtain the final form of the wetting boundary conditions on Γ_t^{sf},

$$\boldsymbol{n}^{sf} \cdot \nabla c_i = h_i, \tag{29}$$

where

$$h_i = -\frac{4}{3\epsilon\Sigma_i}\left(6\gamma_{is}c_i(1 - c_i) + c_j c_k G + c_1 c_2 c_3 \frac{\partial G}{\partial c_i} + H\right), \quad i, j, k = 1, 2, 3, \ \{j, k\} \neq i \text{ and } j \neq k. \tag{30}$$

When (c_1, c_2, c_3) equals $(1, 0, 0)$, $(0, 1, 0)$ and $(0, 0, 1)$ some of the rational functions given by Eq. (28) lead to the result $0/0$ which is undefined. In our implementation, we have used the definition $0/0 = 0$. Our derivation of the wetting boundary conditions differs from that in [47], which was based on a gradient projection method.

Remark 2.3. Let us consider a subset of Γ_t^{sf} where only two fluids meet the solid. If all solid-fluid surface tensions are equal, i.e., $\gamma_{1s} = \gamma_{2s} = \gamma_{3s}$, then Eq. (29) simplifies to the free-flux phase field boundary conditions. To prove this, let us assume $c_3 = 0$ at the subset of Γ_t^{sf} where only two fluids meet the solid. In that case, Eqs. (18) and (26) respectively simplify to

$$R|_{c_3=0} = \gamma_{1s}(3c_1^2 - 2c_1^3) + \gamma_{1s}(3c_2^2 - 2c_2^3) \tag{31}$$

and

$$G|_{c_3=0} = 6\gamma_{1s}, \tag{32}$$

where we have used Eq. (5). Substituting Eqs. (31) and (32) in Eq. (23) with subsequent simplification gives us

$$H|_{c_3=0} = -\frac{\delta}{6} c_1 c_2 \left(\frac{6\gamma_{1s}}{\Sigma_1} + \frac{6\gamma_{1s}}{\Sigma_2} + \frac{G|_{c_3=0}}{\Sigma_3}\right) = -6\gamma_{1s} c_1 c_2. \tag{33}$$

Upon substitution of Eqs. (31), (32) and (33) in Eq. (29), we get $\boldsymbol{n}^{sf} \cdot \nabla c_1 = 0$, $\boldsymbol{n}^{sf} \cdot \nabla c_2 = 0$ and $\boldsymbol{n}^{sf} \cdot \nabla c_3 = 0$. Eq. (33) shows that the function G in Eq. (21) is a necessity, as its omission will not yield free-flux phase field boundary conditions. We have exemplified our proof with $c_3 = 0$. But our proof will also work when $c_1 = 0$ or $c_2 = 0$.

Remark 2.4. In the case of two immiscible fluids, Eq. (29) simplifies to standard wetting boundary conditions in two-fluid mixtures [33]. In this case, Eq. (29) can be rewritten by assuming $c_3 = 0, c_1 = c$ and $c_2 = 1 - c \ \forall c \in [0, 1]$. Now, we no longer assume all solid-fluid surface tensions are equal. In this case, Eqs. (26) and (23) respectively simplify to

$$G|_{c_3=0} = 3\left(\frac{\gamma_{1s}\Sigma_2 + \gamma_{2s}\Sigma_1}{\gamma_{12}}\right) \tag{34}$$

and

$$H|_{c_3=0} = -\frac{3c(1-c)}{\gamma_{12}}\left(\gamma_{12}\left(\gamma_{1s}+\gamma_{2s}\right)+(\gamma_{13}-\gamma_{23})(\gamma_{2s}-\gamma_{1s})\right), \tag{35}$$

where we have used Eq. (5). The algebraic manipulations required to prove Eq. (35) from Eq. (23) are non-trivial. We perform these manipulations via symbolic computations in MATLAB; see Appendix A for the MATLAB script. Substitution of Eqs. (35) and (34) in Eq. (29) with subsequent simplification yields

$$\boldsymbol{n}^{sf}\cdot\nabla c = \frac{4}{\epsilon}\left(\frac{\gamma_{2s}-\gamma_{1s}}{\gamma_{12}}\right)c(1-c). \tag{36}$$

Using the Young's relation from Eq. (19), we can rewrite Eq. (36) as

$$\boldsymbol{n}^{sf}\cdot\nabla c = \frac{4}{\epsilon}\cos\theta_{12}c(1-c). \tag{37}$$

This proof shows that when one fluid is not present, our boundary conditions reduce to standard wetting boundary conditions for a two-fluid mixture.

2.3. Governing equations of solid mechanics

The solid motion is described by the linear momentum balance equation written in the Lagrangian frame as

$$\rho_0^s\,\partial_t^2\boldsymbol{u}\big|_{\boldsymbol{X}} = \nabla_{\boldsymbol{X}}\cdot\boldsymbol{P}+\rho_0^s\boldsymbol{f}^s, \tag{38}$$

where ρ_0^s is the mass density of the solid in the referential configuration, $\boldsymbol{u}$ is the displacement of solid, $\boldsymbol{P}$ is the first Piola-Kirchhoff stress tensor and $\boldsymbol{f}^s$ is the body force on the solid per unit mass. A compressible neo-Hookean model with dilatational penalty [48] is adopted as the constitutive equation of the solid. With this constitutive model, the strain energy density function W for the solid is defined by

$$W = \frac{\mu}{2}\left(J^{-2/d}\,\mathrm{tr}(\boldsymbol{C})-d\right)+\frac{\kappa}{2}\left(\frac{1}{2}\left(J^2-1\right)-\ln J\right), \tag{39}$$

where μ and κ are the shear and bulk moduli of the solid, $\boldsymbol{I}$ is the identity tensor, $\boldsymbol{C}$ is the right Cauchy-Green deformation tensor with $\boldsymbol{C}=\boldsymbol{F}^T\boldsymbol{F}$ and $\mathrm{tr}(\boldsymbol{C})$ denotes the trace of $\boldsymbol{C}$. The bulk and shear moduli are computed as $\kappa=\frac{E}{3(1-2\nu)}$ and $\mu=\frac{E}{2(1+\nu)}$, where E is the Young's modulus of the solid and ν is the Poisson's ratio. The second Piola-Kirchhoff stress tensor $\boldsymbol{S}$ is computed from W as

$$\boldsymbol{S}=\frac{\partial W}{\partial \boldsymbol{E}}=\mu J^{-2/d}\left(\boldsymbol{I}-\frac{1}{d}\,\mathrm{tr}(\boldsymbol{C})\boldsymbol{C}^{-1}\right)+\frac{\kappa}{2}(J^2-1)\boldsymbol{C}^{-1}, \tag{40}$$

where $\boldsymbol{E}$ is the Green-Lagrange strain tensor given by $\boldsymbol{E}=(\boldsymbol{C}-\boldsymbol{I})/2$. The first and second Piola-Kirchhoff stress tensors are related by $\boldsymbol{P}=\boldsymbol{F}\boldsymbol{S}$ while the Cauchy stress tensor is defined by $\boldsymbol{\sigma}^s := J^{-1}\boldsymbol{P}\boldsymbol{F}^T$.

For the solid mechanics equations presented in Eq. (38), we furnish suitable initial conditions by assuming the initial solid displacement and initial solid velocity to be zero. For simplicity, we assume here that the solid is immersed into the fluid and no part of the solid boundary coincides with an external boundary of the computational domain. Thus, we do not need boundary conditions for the solid domain and we will focus on the fluid-solid interface conditions here. If the boundary conditions in our numerical computations are different, we accordingly incorporate them in our formulation.

2.4. Fluid-solid interface conditions

We impose strong kinematic compatibility at the fluid-solid interface Γ_t^{sf},

$$\boldsymbol{v} = \frac{\partial \boldsymbol{u}}{\partial t} \circ \widehat{\boldsymbol{\phi}}^{-1}. \tag{41}$$

Additionally, we impose that the fluid and solid tractions are balanced with the traction induced by the solid-fluid surface tension at Γ_t^{sf} [22]. This can be expressed by

$$\boldsymbol{\sigma}^f \boldsymbol{n}^{sf} + \boldsymbol{\sigma}^s \boldsymbol{n}^s = \nabla_\Gamma \cdot \boldsymbol{\sigma}^{sf}, \tag{42}$$

where $\boldsymbol{n}^s$ is the unit outward normal vector to the solid boundary in the spatial domain, $\boldsymbol{\sigma}^{sf}$ is the stress tensor accounting for the solid-fluid surface tension at Γ_t^{sf} and ∇_Γ is the surface gradient [49, 50] on Γ_t^{sf} defined by $\nabla_\Gamma = \boldsymbol{P}_\Gamma \nabla$. Here, $\boldsymbol{P}_\Gamma = \boldsymbol{I} - \boldsymbol{n}^{sf} \otimes \boldsymbol{n}^{sf}$ is the surface projection tensor, defined as the projection on the tangent plane of Γ_t^{sf}. In elasto-capillarity, the traction induced by the solid-fluid surface tension avoids the singularity at the contact line in the sharp-interface limit; see [22] for more details. Since we neglected the Shuttleworth effect, we use $\boldsymbol{\sigma}^{sf} = \gamma_{sf} \boldsymbol{P}_\Gamma$ which is a simplified form of the Boussinesq surface fluid model [51]. With this definition, the right-hand side of Eq. (42) can be written as

$$\begin{aligned}
\nabla_\Gamma \cdot \boldsymbol{\sigma}^{sf} &= \nabla_\Gamma \cdot (\gamma_{sf} \boldsymbol{P}_\Gamma), \\
&= \gamma_{sf} \nabla_\Gamma \cdot \boldsymbol{P}_\Gamma + \boldsymbol{P}_\Gamma \nabla_\Gamma \gamma_{sf}, \\
&= -\gamma_{sf} \nabla_\Gamma \cdot \left(\boldsymbol{n}^{sf} \otimes \boldsymbol{n}^{sf} \right) + \boldsymbol{P}_\Gamma \boldsymbol{P}_\Gamma \nabla \gamma_{sf}, \\
&= -\gamma_{sf} \left(\boldsymbol{n}^{sf} \cdot \nabla_\Gamma \boldsymbol{n}^{sf} + \nabla_\Gamma \cdot \boldsymbol{n}^{sf} \boldsymbol{n}^{sf} \right) + \boldsymbol{P}_\Gamma \nabla \gamma_{sf}, \\
&= \gamma_{sf} \kappa^{sf} \boldsymbol{n}^{sf} + \nabla_\Gamma \gamma_{sf},
\end{aligned} \tag{43}$$

where $\kappa^{sf} = -\nabla_\Gamma \cdot \boldsymbol{n}^{sf}$ is the additive curvature ($d - 1$ times the mean curvature) of the interface. The fourth and fifth steps in Eq. (43) follow from the properties $\boldsymbol{P}_\Gamma \boldsymbol{P}_\Gamma = \boldsymbol{P}_\Gamma$ and $\boldsymbol{n}^{sf} \cdot \nabla_\Gamma \boldsymbol{n}^{sf} = 0$, respectively.

3. Numerical formulation

3.1. Arbitrary Lagrangian-Eulerian formulation of the fluid mechanics problem

We adopt a boundary-fitted technique with matching discretization at the fluid-solid interface. We solve the fluid and solid equations in the Arbitrary Lagrangian-Eulerian (ALE) and Lagrangian descriptions, respectively. In ALE description, the temporal and spatial derivatives are taken, respectively, with respect to the referential and spatial domains. This makes the adoption of classical semi-discrete methods with finite-difference-in-time treatments directly applicable to moving boundary problems [7]. To maintain mesh conformity throughout the domain, we update the fluid mesh to accommodate the solid motion. The fluid mesh update is performed by solving successive fictitious linear elasticity problems [52]. Using the techniques presented in [38, 53], we write Eq. (7) in the ALE description as

$$\nabla \cdot \boldsymbol{v} = 0, \tag{44a}$$

$$\rho \Big(\partial_t \boldsymbol{v}|_{\widehat{\boldsymbol{x}}} + (\boldsymbol{v} - \widehat{\boldsymbol{v}}) \cdot \nabla \boldsymbol{v} \Big) = \nabla \cdot \boldsymbol{\sigma}^f + \rho \boldsymbol{f}, \tag{44b}$$

$$\partial_t c_i|_{\widehat{\boldsymbol{x}}} + (\boldsymbol{v} - \widehat{\boldsymbol{v}}) \cdot \nabla c_i = \nabla \cdot \left(\frac{M_0}{\Sigma_i} \nabla \mu_i \right); \; i = 1, 2, \tag{44c}$$

$$\mu_i = -\frac{3}{4} \epsilon \Sigma_i \Delta c_i + \frac{12}{\epsilon} \Sigma_i c_i (1 - c_i)(1 - 2c_i) - \frac{12\delta}{\epsilon} c_1 c_2 (1 - c_1 - c_2); \; i = 1, 2, \tag{44d}$$

where $\widehat{\boldsymbol{v}}$ is the velocity of fluid mesh motion which can be obtained from the mapping $\widehat{\boldsymbol{\phi}}$.

3.2. Variational formulation of the fluid-structure interaction problem at the continuous level

3.2.1. Fluid mechanics problem

Here, we derive the weak form of Eq. (44). In this derivation, we ignore the boundary terms on Γ_t^{sf} arising from the linear momentum balance. These pertain to the fluid-solid coupling and will be discussed later. For the linear momentum balance equation, we will assume boundary conditions on Γ_t^f that correspond to either homogeneous Dirichlet conditions or zero-traction conditions. This assumption renders vanishing boundary terms on Γ_t^f for the momentum balance equation. Let $L^2(\Omega_t^f)$ be a functional space of scalar-valued functions that are square-integrable on Ω_t^f. The trial function space for the fluid pressure is defined as

$$\mathcal{V}^p = \left\{ p \mid p \in L^2(\Omega_t^f), \int_{\Omega_t^f} p d\Omega_t^f = 0 \right\} \tag{45}$$

and the weight function space $\mathcal{W}^p$ is identical to $\mathcal{V}^p$. Additionally, we define $\mathcal{V}^{c_1}$, $\mathcal{V}^{c_2}$, $\mathcal{V}^{\mu_1}$ and $\mathcal{V}^{\mu_2}$ to be the trial function spaces for c_1, c_2, μ_1 and μ_2, respectively. Here, $\mathcal{V}^{c_1} = \mathcal{V}^{c_2} = \mathcal{V}^{\mu_1} = \mathcal{V}^{\mu_2} = \mathcal{H}^1(\Omega_t^f)$, where $\mathcal{H}^1(\Omega_t^f)$ is the Sobolev space of square-integrable functions with square-integrable first derivatives in the domain Ω_t^f. Let the weight functions $\mathcal{W}^{c_1}$, $\mathcal{W}^{c_2}$, $\mathcal{W}^{\mu_1}$ and $\mathcal{W}^{\mu_2}$ be identical to their respective trial function spaces. We define $\mathcal{V}^v \subset [\mathcal{H}^1(\Omega_t^f)]^d$ as a trial function space for $\boldsymbol{v}$ which satisfies Dirichlet boundary conditions. The corresponding weight function space $\mathcal{W}^v$ for $\boldsymbol{v}$ is identical to $\mathcal{V}^v$, except that all restrictions on the Dirichlet boundary are homogeneous. The variational formulation for the fluid mechanics problem is now stated as follows: find $p \in \mathcal{V}^p, \boldsymbol{v} \in \mathcal{V}^v$, $c_1 \in \mathcal{V}^{c_1}$, $c_2 \in \mathcal{V}^{c_2}$, $\mu_1 \in \mathcal{V}^{\mu_1}$ and $\mu_2 \in \mathcal{V}^{\mu_2}$ such that $\forall w^1 \in \mathcal{W}^p$, $\boldsymbol{w}^2 \in \mathcal{W}^v$, $w^3 \in \mathcal{W}^{c_1}$, $w^4 \in \mathcal{W}^{c_2}$, $w^5 \in \mathcal{W}^{\mu_1}$ and $w^6 \in \mathcal{W}^{\mu_2}$,

$$\begin{aligned}
&B^f\big((w^1,\boldsymbol{w}^2,w^3,w^4,w^5,w^6),(p,\boldsymbol{v},c_1,c_2,\mu_1,\mu_2);\hat{\boldsymbol{v}}\big) \\
&\quad= \int_{\Omega_t^f} w^1 \nabla\cdot\boldsymbol{v} d\Omega_t^f + \int_{\Omega_t^f} \boldsymbol{w}^2\cdot\rho\Big(\partial_t\boldsymbol{v}|_{\widehat{\boldsymbol{x}}} + (\boldsymbol{v}-\widehat{\boldsymbol{v}})\cdot\nabla\boldsymbol{v}\Big) d\Omega_t^f \\
&\quad+ \int_{\Omega_t^f} \nabla\boldsymbol{w}^2 : \boldsymbol{\sigma}^f d\Omega_t^f - \int_{\Omega_t^f} \boldsymbol{w}^2\cdot\rho\boldsymbol{f} d\Omega_t^f \\
&\quad+ \int_{\Omega_t^f} w^3\,\partial_t c_1|_{\widehat{\boldsymbol{x}}}\, d\Omega_t^f + \int_{\Omega_t^f} w^3(\boldsymbol{v}-\hat{\boldsymbol{v}})\cdot\nabla c_1 d\Omega_t^f + \int_{\Omega_t^f} \frac{M_0}{\Sigma_1}\nabla w^3\cdot\nabla\mu_1 d\Omega_t^f \\
&\quad+ \int_{\Omega_t^f} w^4\,\partial_t c_2|_{\widehat{\boldsymbol{x}}}\, d\Omega_t^f + \int_{\Omega_t^f} w^4(\boldsymbol{v}-\hat{\boldsymbol{v}})\cdot\nabla c_2 d\Omega_t^f + \int_{\Omega_t^f} \frac{M_0}{\Sigma_2}\nabla w^4\cdot\nabla\mu_2 d\Omega_t^f \\
&\quad+ \int_{\Omega_t^f} w^5\mu_1 d\Omega_t^f - \int_{\Omega_t^f} \frac{3}{4}\epsilon\Sigma_1\nabla w^5\cdot\nabla c_1 d\Omega_t^f + \int_{\Gamma_t^{sf}} \frac{3}{4}\epsilon\Sigma_1 w^5 h_1 d\Gamma_t \\
&\quad- \int_{\Omega_t^f} w^5\left(\frac{12}{\epsilon}\Sigma_1 c_1(1-c_1)(1-2c_1) - \frac{12\delta}{\epsilon}c_1c_2(1-c_1-c_2)\right) d\Omega_t^f \\
&\quad+ \int_{\Omega_t^f} w^6\mu_2 d\Omega_t^f - \int_{\Omega_t^f} \frac{3}{4}\epsilon\Sigma_2\nabla w^6\cdot\nabla c_2 d\Omega_t^f + \int_{\Gamma_t^{sf}} \frac{3}{4}\epsilon\Sigma_2 w^6 h_2 d\Gamma_t \\
&\quad- \int_{\Omega_t^f} w^6\left(\frac{12}{\epsilon}\Sigma_2 c_2(1-c_2)(1-2c_2) - \frac{12\delta}{\epsilon}c_1c_2(1-c_1-c_2)\right) d\Omega_t^f = 0
\end{aligned} \tag{46}$$

Eq. (46) imposes weakly the governing equations (44) as well as the boundary conditions (10)–(14) and (29). The weak imposition of the boundary conditions (29) was facilitated by our splitting

of the original fourth-order phase field equation into two second-order equations, i.e., Eqs. (7c) and (7d) or Eqs. (44c) and (44d). The split of fourth-order equations into a system of second-order equations has been frequently used in the literature because it allows the use of classical $\mathcal{C}^0$-continuous finite elements and because the imposition of boundary conditions is simple. However, the use of IGA [39, 40] permits to use basis functions with higher-order inter-element continuity on mapped domains, and thus, a formulation in which Eq. (44d) is substituted in (44c) is possible. The latter approach (not pursued here) is usually called direct or primal formulation. Recent research [54] has shown that a judicious modification of the usual weak form of the direct formulation also permits simultaneous weak imposition of Eqs. (12) and (29). The formulation proposed in [54] is as simple as the split formulation, converges at optimal rate, and avoids the use of global degrees of freedom for the chemical potentials. The method proposed in [54] also avoids the appearance of non-physical solutions that occurs when the split method is employed on concave geometries [55]. Reference [55] also shows that the split and direct formulations of fourth or higher-order PDEs converge to the same numerical solution on convex geometries. We employ convex geometries in our numerical examples, and hence, we do not expect significant differences between the numerical solutions from direct and split methods.

The spatial discretization of the tNSCH model using equal order function spaces for fluid velocity $\boldsymbol{v}$ and pressure p requires stabilization. Stabilization techniques like the Variational Multiscale Method (VMS) [56] or SUPG/PSPG [57, 58]) have been commonly employed in the literature. In the current work, we adopt VMS. With this scheme, the trial and weight function spaces of velocity and pressure are decomposed into coarse and fine scale subspaces, i.e., $\mathcal{V}^p = \overline{\mathcal{V}}^p \oplus \mathcal{V}^{p\prime}$, $\mathcal{V}^v = \overline{\mathcal{V}}^v \oplus \mathcal{V}^{v\prime}$, $\mathcal{W}^p = \overline{\mathcal{W}}^p \oplus \mathcal{W}^{p\prime}$ and $\mathcal{W}^v = \overline{\mathcal{W}}^v \oplus \mathcal{W}^{v\prime}$. Accordingly, $\boldsymbol{v} \in \mathcal{V}^v$, $p \in \mathcal{V}^p$, $w^1 \in \mathcal{W}^p$ and $\boldsymbol{w}^2 \in \mathcal{W}^v$ can be split into a coarse and fine scale component as, $p = \overline{p} + p'$, $\boldsymbol{v} = \overline{\boldsymbol{v}} + \boldsymbol{v}'$, $w^1 = \overline{w}^1 + w^{1\prime}$ and $\boldsymbol{w}^2 = \overline{\boldsymbol{w}}^2 + \boldsymbol{w}^{2\prime}$ with $\overline{p} \in \overline{\mathcal{V}}^p$, $\overline{\boldsymbol{v}} \in \overline{\mathcal{V}}^v$, $p' \in \mathcal{V}^{p\prime}$, $\boldsymbol{v}' \in \mathcal{W}^{v\prime}$, $\overline{w}^1 \in \overline{\mathcal{W}}^p$, $w^{1\prime} \in \mathcal{W}^{p\prime}$, $\overline{\boldsymbol{w}}^2 \in \overline{\mathcal{W}}^v$ and $\boldsymbol{w}^{2\prime} \in \mathcal{W}^{v\prime}$.

3.2.2. Solid mechanics problem

Here, we derive the weak form of the solid mechanics problem. In the derivation, we ignore the boundary terms on Γ_t^{sf}. We define $\mathcal{V}^s \subset [\mathcal{H}^1(\Omega_0^s)]^d$ to be a trial function space, where Ω_0^s is the solid domain in the referential configuration. The corresponding weight function space $\mathcal{W}^s$ is identical to $\mathcal{V}^s$. The variational formulation for the solid mechanics problem can be stated as follows: find $\boldsymbol{u} \in \mathcal{V}^s$ such that $\forall \boldsymbol{w}^s \in \mathcal{W}^s$,

$$B^s(\boldsymbol{w}^s, \boldsymbol{u}) = \int_{\Omega_0^s} \left(\boldsymbol{w}^s \cdot \rho_0^s \partial_t^2 \, \boldsymbol{u}|_{\boldsymbol{X}} + \nabla_{\boldsymbol{X}} \boldsymbol{w}^s : \boldsymbol{P} - \boldsymbol{w}^s \cdot \rho_0^s \boldsymbol{f}^s \right) d\Omega_0^s = 0. \tag{47}$$

Eq. (47) is devoid of boundary terms because we assumed the solid to be immersed in the fluid. If the solid is not fully immersed in the fluid, additional boundary terms may need to be added.

3.2.3. Fluid mesh motion

We solve successive fictitious linear elasticity equations to update the fluid mesh, which is subject to Dirichlet boundary conditions from the solid displacement [7]. We denote the displacement of the reference domain as

$$\widehat{\boldsymbol{u}}(\widehat{\boldsymbol{x}}, t) = \widehat{\boldsymbol{\phi}}(\widehat{\boldsymbol{x}}, t) - \widehat{\boldsymbol{x}}. \tag{48}$$

We determine $\widehat{\boldsymbol{\phi}}(\widehat{\boldsymbol{x}}, t)$ from the equation

$$\widehat{\boldsymbol{\phi}}(\widehat{\boldsymbol{x}}, t) = \widehat{\boldsymbol{\phi}}(\widehat{\boldsymbol{x}}, \widetilde{t}) + \widehat{\boldsymbol{u}}(\widehat{\boldsymbol{x}}, t) - \widehat{\boldsymbol{u}}(\widehat{\boldsymbol{x}}, \widetilde{t}), \tag{49}$$

where $\widetilde{t} < t$. We define $\boldsymbol{u}^m = \widehat{\boldsymbol{u}}(\widehat{\boldsymbol{x}}, t) - \widehat{\boldsymbol{u}}(\widehat{\boldsymbol{x}}, \widetilde{t})$ and compute an approximation to it by solving a fictitious linear elastic motion.

Let $\Omega^f_{\widetilde{t}}$ be the referential configuration of the fluid domain Ω^f_0 at $\widetilde{t}$. Similarly, we define $\Gamma_{\widetilde{t}}$ as the mapping of the fluid-solid interface in the referential configuration at time $\widetilde{t}$. Our unknown $\boldsymbol{u}^m$ is subject to Dirichlet boundary conditions given by $\boldsymbol{u}^m = \boldsymbol{u} \circ \widehat{\boldsymbol{\phi}}^{-1}\Big|_t - \boldsymbol{u} \circ \widehat{\boldsymbol{\phi}}^{-1}\Big|_{\widetilde{t}}$ on $\Gamma_{\widetilde{t}}$. We now define $\mathcal{V}^m \subset [\mathcal{H}^1(\Omega^f_{\widetilde{t}})]^d$ as a trial function space satisfying Dirichlet boundary conditions. The corresponding weight function space $\mathcal{W}^m$ is identical to $\mathcal{V}^m$ except that all restrictions on the Dirichlet boundary are homogeneous. The variational formulation of the fluid mesh motion can now be stated as follows: find $\boldsymbol{u}^m \in \mathcal{V}^m$ such that $\forall \boldsymbol{w}^m \in \mathcal{W}^m$

$$B^m(\boldsymbol{w}^m, \boldsymbol{u}^m) = \int_{\Omega^f_{\widetilde{t}}} \nabla^s_{\widetilde{\boldsymbol{x}}} \boldsymbol{w}^m : 2\mu^m \nabla^s_{\widetilde{\boldsymbol{x}}} \boldsymbol{u}^m d\Omega^f_{\widetilde{t}} + \int_{\Omega^f_{\widetilde{t}}} \nabla_{\widetilde{\boldsymbol{x}}} \cdot \boldsymbol{w}^m \lambda^m \nabla_{\widetilde{\boldsymbol{x}}} \cdot \boldsymbol{u}^m d\Omega^f_{\widetilde{t}} = 0, \tag{50}$$

where $\nabla_{\widetilde{\boldsymbol{x}}}$ is the gradient operator on $\Omega^f_{\widetilde{t}}$. Additionally, μ^m and λ^m are the Lamé parameters of the fictitious elastic problem, which are suitably selected to preserve the quality of the fluid mesh.

3.2.4. Coupled fluid-structure interaction problem

The variational formulation of the coupled FSI problem can be stated as follows: find $\overline{p} \in \overline{\mathcal{V}}^p$, $p' \in \mathcal{W}^{p'}$, $\overline{\boldsymbol{v}} \in \overline{\mathcal{V}}^v$, $\boldsymbol{v}' \in \mathcal{V}^{v'}$, $c_1 \in \mathcal{V}^{c_1}$, $c_2 \in \mathcal{V}^{c_2}$, $\mu_1 \in \mathcal{V}^{\mu_1}$, $\mu_2 \in \mathcal{V}^{\mu_2}$, $\boldsymbol{u} \in \mathcal{V}^s$ and $\boldsymbol{u}^m \in \mathcal{V}^m$ such that $\forall \overline{w}^1 \in \overline{\mathcal{W}}^p$, $\overline{\boldsymbol{w}}^2 \in \overline{\mathcal{W}}^v$, $w^3 \in \mathcal{W}^{c_1}$, $w^4 \in \mathcal{W}^{c_2}$, $w^5 \in \mathcal{W}^{\mu_1}$, $w^6 \in \mathcal{W}^{\mu_2}$, $\boldsymbol{w}^s \in \mathcal{W}^s$ and $\boldsymbol{w}^m \in \mathcal{W}^m$,

$$\begin{aligned} &B^f\left(\left(\overline{w}^1, \overline{\boldsymbol{w}}^2, w^3, w^4, w^5, w^6\right), \left(\overline{p} + p', \overline{\boldsymbol{v}} + \boldsymbol{v}', c_1, c_2, \mu_1, \mu_2\right); \hat{\boldsymbol{v}}\right) + B^s(\boldsymbol{w}^s, \boldsymbol{u}) + B^m(\boldsymbol{w}^m, \boldsymbol{u}^m) \\ &= T^f\left(\overline{\boldsymbol{w}}^2, \left(\overline{p} + p', \overline{\boldsymbol{v}} + \boldsymbol{v}', c_1, c_2\right)\right) + T^s(\boldsymbol{w}^s, \boldsymbol{u}), \end{aligned} \tag{51}$$

where T^f and T^s include the contributions of the fluid and solid tractions at the fluid-solid interface, respectively. T^f and T^s are given by

$$T^f\left(\overline{\boldsymbol{w}}^2, \left(\overline{p} + p', \overline{\boldsymbol{v}} + \boldsymbol{v}', c_1, c_2\right)\right) = \int_{\Gamma^{sf}_t} \boldsymbol{\sigma}^f \boldsymbol{n}^{sf} \cdot \overline{\boldsymbol{w}}^2 d\Gamma_t \tag{52}$$

and

$$T^s(\boldsymbol{w}^s, \boldsymbol{u}) = \int_{\Gamma^{sf}_0} \boldsymbol{P}\boldsymbol{n}^s_0 \cdot \boldsymbol{w}^s d\Gamma^{sf}_0 = \int_{\Gamma^{sf}_t} \boldsymbol{\sigma}^s \boldsymbol{n}^s \cdot \left(\boldsymbol{w}^s \circ \widehat{\boldsymbol{\phi}}^{-1}\right) d\Gamma_t. \tag{53}$$

To enforce traction balance as in Eq. (42), we take [7]

$$\overline{\boldsymbol{w}}^2 = \boldsymbol{w}^s \circ \widehat{\boldsymbol{\phi}}^{-1} \text{ on } \Gamma^{sf}_t. \tag{54}$$

Due to our splitting of the fluid velocity $\boldsymbol{v}$ into a coarse and fine scale component, we reformulate the kinematic boundary condition in Eq. (41) as

$$\overline{\boldsymbol{v}} = \frac{\partial \boldsymbol{u}}{\partial t} \circ \widehat{\boldsymbol{\phi}}^{-1}. \tag{55}$$

Using Eq. (42) and $\boldsymbol{\sigma}^{sf} = \gamma_{sf}\boldsymbol{P}_\Gamma$ [49], we obtain

$$
\begin{aligned}
&T^f\left(\overline{\boldsymbol{w}}^2, \left(\overline{p}+p', \overline{\boldsymbol{v}}+\boldsymbol{v}', c_1, c_2\right)\right) + T^s(\boldsymbol{w}^s, \boldsymbol{u}) \\
&= \int_{\Gamma_t^{sf}} \left(\boldsymbol{\sigma}^f \boldsymbol{n}^{sf} + \boldsymbol{\sigma}^s \boldsymbol{n}^s\right) \cdot \overline{\boldsymbol{w}}^2 d\Gamma_t, \\
&= \int_{\Gamma_t^{sf}} \nabla_\Gamma \cdot (\gamma_{sf}\boldsymbol{P}_\Gamma) \cdot \overline{\boldsymbol{w}}^2 d\Gamma_t, \\
&= -\int_{\Gamma_t^{sf}} \gamma_{sf}\boldsymbol{P}_\Gamma : \nabla_\Gamma \overline{\boldsymbol{w}}^2 d\Gamma_t + \int_{\partial\Gamma_t^{sf}} \gamma_{sf}\overline{\boldsymbol{w}}^2 \cdot \boldsymbol{P}_\Gamma \boldsymbol{t} d(\partial\Gamma_t), \\
&= -\int_{\Gamma_t^{sf}} \gamma_{sf}\boldsymbol{P}_\Gamma : \nabla_\Gamma \overline{\boldsymbol{w}}^2 d\Gamma_t + \int_{\partial\Gamma_t^{sf}} \gamma_{sf}\boldsymbol{t} \cdot \overline{\boldsymbol{w}}^2 d(\partial\Gamma_t).
\end{aligned}
\tag{56}
$$

where the last step in Eq. (56) follows from the property $\left(\boldsymbol{n}^{sf} \otimes \boldsymbol{n}^{sf}\right)\boldsymbol{t} = 0$ which allows us to conclude $\overline{\boldsymbol{w}}^2 \cdot \boldsymbol{P}_\Gamma \boldsymbol{t} = \boldsymbol{t} \cdot \overline{\boldsymbol{w}}^2$. In Eq. (56), $\boldsymbol{t}$ is a unit vector tangent to Γ_t^{sf} and normal to $\partial\Gamma_t^{sf}$. We replace the sum of the fluid and solid tractions at the fluid-solid interface in the variational formulation of Eq. (51) with the right-hand side of Eq. (56). Following [22], we neglect the term containing $\boldsymbol{t} \cdot \overline{\boldsymbol{w}}^2$ in Eq. (56).

Remark 3.1. The first term in the final step on the right hand side of Eq. (56) can be alternatively written in two different forms. For the first form, we simplify this term as follows

$$
\begin{aligned}
-\int_{\Gamma_t^{sf}} \gamma_{sf}\boldsymbol{P}_\Gamma : \nabla_\Gamma \overline{\boldsymbol{w}}^2 d\Gamma_t &= -\int_{\Gamma_t^{sf}} \gamma_{sf}\boldsymbol{P}_\Gamma : \nabla \overline{\boldsymbol{w}}^2 \boldsymbol{P}_\Gamma d\Gamma_t \\
&= -\int_{\Gamma_t^{sf}} \gamma_{sf}\boldsymbol{P}_\Gamma \boldsymbol{P}_\Gamma^T : \nabla \overline{\boldsymbol{w}}^2 d\Gamma_t \\
&= -\int_{\Gamma_t^{sf}} \gamma_{sf}\boldsymbol{P}_\Gamma : \nabla \overline{\boldsymbol{w}}^2 d\Gamma_t.
\end{aligned}
\tag{57}
$$

Eq. (57) is identical to the one employed in [50] for two-fluid mixtures and involves no surface gradients in the variational formulation. The first and the last lines in Eq. (57) follow from the properties $\nabla_\Gamma \overline{\boldsymbol{w}}^2 = \nabla \overline{\boldsymbol{w}}^2 \boldsymbol{P}_\Gamma$ and $\boldsymbol{P}_\Gamma \boldsymbol{P}_\Gamma^T = \boldsymbol{P}_\Gamma$, respectively.

For the second form, we define an identity function as $\mathbf{I_d}(\boldsymbol{x}) := \boldsymbol{x}$ for $\boldsymbol{x} \in \Gamma_t^{sf}$ satisfying $\boldsymbol{P}_\Gamma = \nabla_\Gamma \mathbf{I_d}$ [50]. In this case, the first term on the right hand side of Eq. (56) can be written as $-\int_{\Gamma_t^{sf}} \gamma_{sf} \nabla_\Gamma \mathbf{I_d} : \nabla_\Gamma \overline{\boldsymbol{w}}^2 d\Gamma_t$, which is identical to the form employed in [22]. The identity function $\mathbf{I_d}$ is also related to κ^{sf} as $\kappa^{sf}\boldsymbol{n}^f = \Delta_\Gamma \mathbf{I_d}$, where Δ_Γ is the surface Laplacian.

Remark 3.2. An alternative approach of including the traction from the solid-fluid surface tension is to transform the left-hand side of Eq. (57) into a volume integral as in the continuum surface methods [59]; see [26, 50] and references therein for more details.

3.3. Semi-discrete formulation of the coupled fluid-structure interaction problem

To obtain the semi-discrete variational formulation, we substitute the functional spaces defined in Sec. 3.2 by finite-dimensional subspaces. We define the discrete trial functional spaces as, $\overline{\mathcal{V}}_h^p \subset \overline{\mathcal{V}}^p$, $\overline{\mathcal{V}}_h^v \subset \overline{\mathcal{V}}^v$, $\mathcal{V}_h^{c_1} \subset \mathcal{V}^{c_1}$, $\mathcal{V}_h^{c_2} \subset \mathcal{V}^{c_2}$, $\mathcal{V}_h^{\mu_1} \subset \mathcal{V}^{\mu_1}$, $\mathcal{V}_h^{\mu_2} \subset \mathcal{V}^{\mu_2}$, $\mathcal{V}_h^s \subset \mathcal{V}^s$ and $\mathcal{V}_h^m \subset \mathcal{V}^m$. We define the corresponding discrete weight function spaces as $\overline{\mathcal{W}}_h^p \subset \overline{\mathcal{W}}^p$, $\overline{\mathcal{W}}_h^v \subset \overline{\mathcal{W}}^v$, $\mathcal{W}_h^{c_1} \subset \mathcal{W}^{c_1}$, $\mathcal{W}_h^{c_2} \subset \mathcal{W}^{c_2}$, $\mathcal{W}_h^{\mu_1} \subset \mathcal{W}^{\mu_1}$, $\mathcal{W}_h^{\mu_2} \subset \mathcal{W}^{\mu_2}$, $\mathcal{W}_h^s \subset \mathcal{W}^s$ and $\mathcal{W}_h^m \subset \mathcal{W}^m$.

Residual based approximations [60] are employed to model the fine-scale components $p', \boldsymbol{v}'$ as

$$\rho \boldsymbol{v}' = -\tau_m \overline{\boldsymbol{R}}_m, \; p' = -\rho \tau_c \overline{R}_c, \tag{58}$$

where, $\overline{\boldsymbol{R}}_m$ and $\overline{R}_c$ are the residuals of the momentum and continuity equations, given by

$$\overline{\boldsymbol{R}}_m = \rho \left(\partial_t \, \overline{\boldsymbol{v}}_h|_{\widehat{\boldsymbol{x}}} + (\overline{\boldsymbol{v}}_h - \widehat{\boldsymbol{v}}_h) \cdot \nabla \overline{\boldsymbol{v}}_h \right) - \nabla \cdot \boldsymbol{\sigma}_h^f - \rho \boldsymbol{f}, \tag{59a}$$

$$\overline{R}_c = \nabla \cdot \overline{\boldsymbol{v}}_h. \tag{59b}$$

In Eq. (59), $\boldsymbol{\sigma}_h^f$ is the discrete counterpart of $\boldsymbol{\sigma}^f$ evaluated from Eq. (8) by replacing p, $\boldsymbol{v}$, c_1 and c_2 with their discrete counterparts, given by $\overline{p}_h$, $\overline{\boldsymbol{v}}_h$, c_{1h} and c_{2h} respectively. The stabilization parameters τ_m and τ_c in Eq. (58) are computed as

$$\tau_m = \left(\frac{4}{(\Delta t)^2} + (\overline{\boldsymbol{v}}_h - \widehat{\boldsymbol{v}}_h) \cdot \boldsymbol{G} (\overline{\boldsymbol{v}}_h - \widehat{\boldsymbol{v}}_h) + C_I \left(\frac{\eta}{\rho} \right)^2 \boldsymbol{G} : \boldsymbol{G} \right)^{-1/2}, \tag{60a}$$

$$\tau_c = \frac{1}{\mathrm{tr}(\boldsymbol{G}) \tau_m}. \tag{60b}$$

In Eq. (60), Δt is the time step, $C_I = \frac{1}{12}$ [23] is a constant and $\boldsymbol{G}$ is the element metric tensor [38], i.e., $G_{ij} = \sum_{k=1}^{d} \frac{\partial \zeta_k}{\partial x_i} \frac{\partial \zeta_k}{\partial x_j}$, where $\frac{\partial \boldsymbol{\zeta}}{\partial \boldsymbol{x}}$ is the inverse Jacobian of the mapping between parametric and physical domains.

The variational formulation of the coupled FSI problem can be stated as follows: find $\overline{p}_h \in \overline{\mathcal{V}}_h^p$, $\overline{\boldsymbol{v}}_h \in \overline{\mathcal{V}}_h^v$, $c_{1h} \in \mathcal{V}_h^{c_1}$, $c_{2h} \in \mathcal{V}_h^{c_2}$, $\mu_{1h} \in \mathcal{V}_h^{\mu_1}$, $\mu_{2h} \in \mathcal{V}_h^{\mu_2}$, $\boldsymbol{u}_h \in \mathcal{V}_h^s$ and $\boldsymbol{u}_h^m \in \mathcal{V}_h^m$ such that $\forall \overline{w}_h^1 \in \overline{\mathcal{W}}_h^p$, $\overline{\boldsymbol{w}}_h^2 \in \overline{\mathcal{W}}_h^v$, $w_h^3 \in \mathcal{W}_h^{c_1}$, $w_h^4 \in \mathcal{W}_h^{c_2}$, $w_h^5 \in \mathcal{W}_h^{\mu_1}$, $w_h^6 \in \mathcal{W}_h^{\mu_2}$, $\boldsymbol{w}_h^s \in \mathcal{W}_h^s$ and $\boldsymbol{w}_h^m \in \mathcal{W}_h^m$

$$\begin{aligned} &B_{VMS}^f\big((\overline{w}_h^1, \overline{\boldsymbol{w}}_h^2, w_h^3, w_h^4, w_h^5, w_h^6), (\overline{p}_h, \overline{\boldsymbol{v}}_h, c_{1h}, c_{2h}, \mu_{1h}, \mu_{2h}); \hat{\boldsymbol{v}}_h\big) + B^s(\boldsymbol{w}_h^s, \boldsymbol{u}_h) + B^m(\boldsymbol{w}_h^m, \boldsymbol{u}_h^m) \\ &= T^{sf}\big(\overline{\boldsymbol{w}}_h^2, (c_{1h}, c_{2h})\big), \end{aligned} \tag{61}$$

where

$$
\begin{aligned}
&B^f_{VMS}\big((\overline{w}^1_h,\overline{\boldsymbol{w}}^2_h,w^3_h,w^4_h,w^5_h,w^6_h),(\overline{p}_h,\overline{\boldsymbol{v}}_h,c_{1h},c_{2h},\mu_{1h},\mu_{2h});\hat{\boldsymbol{v}}_h\big)=\\
&\quad\int_{\Omega^f_t}\overline{w}^1_h\nabla\cdot\overline{\boldsymbol{v}}_h d\Omega^f_t+\int_{\Omega^f_t}\overline{\boldsymbol{w}}^2_h\cdot\rho\Big(\partial_t\,\overline{\boldsymbol{v}}_h|_{\widehat{\boldsymbol{x}}}+(\overline{\boldsymbol{v}}_h-\hat{\boldsymbol{v}}_h)\cdot\nabla\overline{\boldsymbol{v}}_h\Big)d\Omega^f_t\\
&\quad+\int_{\Omega^f_t}\nabla\overline{\boldsymbol{w}}^2_h:\boldsymbol{\sigma}^f_h d\Omega^f_t-\int_{\Omega^f_t}\overline{\boldsymbol{w}}^2_h\cdot\rho\boldsymbol{f}d\Omega^f_t\\
&\quad+\int_{\Omega^f_t}w^3_h\Big(\partial_t c_{1h}|_{\widehat{\boldsymbol{x}}}+(\overline{\boldsymbol{v}}_h-\hat{\boldsymbol{v}}_h)\cdot\nabla c_{1h}\Big)d\Omega^f_t+\int_{\Omega^f_t}\frac{M_0}{\Sigma_1}\nabla w^3_h\cdot\nabla\mu_{1h}d\Omega^f_t\\
&\quad+\int_{\Omega^f_t}w^4_h\Big(\partial_t c_{2h}|_{\widehat{\boldsymbol{x}}}+(\overline{\boldsymbol{v}}_h-\hat{\boldsymbol{v}}_h)\cdot\nabla c_{2h}\Big)d\Omega^f_t+\int_{\Omega^f_t}\frac{M_0}{\Sigma_2}\nabla w^4_h\cdot\nabla\mu_{2h}d\Omega^f_t\\
&\quad+\int_{\Omega^f_t}w^5_h\mu_{1h}d\Omega^f_t-\int_{\Omega^f_t}\frac{3}{4}\epsilon\Sigma_1\nabla w^5_h\cdot\nabla c_{1h}d\Omega^f_t+\int_{\Gamma^{sf}_t}w^5_h\frac{3}{4}\epsilon\Sigma_1 h_1 d\Gamma_t\\
&\quad-\int_{\Omega^f_t}w^5_h\Big(\frac{12}{\epsilon}\Sigma_1 c_{1h}(1-c_{1h})(1-2c_{1h})-\frac{12\delta}{\epsilon}c_{1h}c_{2h}(1-c_{1h}-c_{2h})\Big)d\Omega^f_t\\
&\quad+\int_{\Omega^f_t}w^6_h\mu_{2h}d\Omega^f_t-\int_{\Omega^f_t}\frac{3}{4}\epsilon\Sigma_2\nabla w^6_h\cdot\nabla c_{2h}d\Omega^f_t+\int_{\Gamma^{sf}_t}w^6_h\frac{3}{4}\epsilon\Sigma_2 h_2 d\Gamma_t\\
&\quad-\int_{\Omega^f_t}w^6_h\Big(\frac{12}{\epsilon}\Sigma_2 c_{2h}(1-c_{2h})(1-2c_{2h})-\frac{12\delta}{\epsilon}c_{1h}c_{2h}(1-c_{1h}-c_{2h})\Big)d\Omega^f_t\\
&\quad+\sum_{e=1}^{n_{el}}\int_{\Omega^{f,e}_t}\tau_m\left((\overline{\boldsymbol{v}}_h-\hat{\boldsymbol{v}}_h)\cdot\nabla\overline{\boldsymbol{w}}^2_h+\frac{\nabla w^1_h}{\rho}\right)\cdot\overline{\boldsymbol{R}}_m d\Omega^f_t\\
&\quad+\sum_{e=1}^{n_{el}}\int_{\Omega^{f,e}_t}\rho\tau_c\overline{R}_c\nabla\cdot\overline{\boldsymbol{w}}^2_h d\Omega^f_t-\sum_{e=1}^{n_{el}}\int_{\Omega^{f,e}_t}\tau_m\overline{\boldsymbol{w}}^2_h\cdot\left(\overline{\boldsymbol{R}}_m\cdot\nabla\overline{\boldsymbol{v}}_h\right)d\Omega^f_t\\
&\quad-\sum_{e=1}^{n_{el}}\int_{\Omega^{f,e}_t}\frac{\nabla\overline{\boldsymbol{w}}^2_h}{\rho}:\left(\tau_m\overline{\boldsymbol{R}}_m\otimes\tau_m\overline{\boldsymbol{R}}_m\right)d\Omega^f_t\\
&\quad-\sum_{e=1}^{n_{el}}\int_{\Omega^{f,e}_t}\frac{\tau_m}{\rho}w^3_h\overline{\boldsymbol{R}}_m\cdot\nabla c_{1h}d\Omega^f_t-\sum_{e=1}^{n_{el}}\int_{\Omega^{f,e}_t}\frac{\tau_m}{\rho}w^4_h\overline{\boldsymbol{R}}_m\cdot\nabla c_{2h}d\Omega^f_t
\end{aligned}
\tag{62}
$$

and

$$
T^{sf}\left(\overline{\boldsymbol{w}}^2_h,(c_{1h},c_{2h})\right)=-\int_{\Gamma^{sf}_t}\gamma_{sf}\boldsymbol{P}_\Gamma:\nabla_\Gamma\overline{\boldsymbol{w}}^2_h d\Gamma_t. \tag{63}
$$

In Eq. (62), n_{el} refers to the total number of elements on the fluid mesh and $\Omega^{f,e}_t$ is the fluid domain occupied by a finite element e at time t. Some assumptions employed to obtain the stabilized variational formulation in Eq. (62) include [60, 61]:

1. $\boldsymbol{v}'=0$ and $p'=0$ on $\Gamma^{sf}_t\cup\Gamma^f_t$.
2. $\int_{\Omega^f_t}\nabla^s\overline{\boldsymbol{w}}^2_h:2\eta\nabla^s\boldsymbol{v}'d\Omega^f_t=0$, which arises from the orthogonality condition of the projection.
3. $\partial_t\boldsymbol{v}'=0$ on Ω^f_t.

The finite-dimensional trial and weight function spaces are defined using splines through the concept of IGA. IGA is a generalization of finite elements that has reached significant success in computational phase-field modeling [62–64] because it permits to define basis functions with controllable

inter-element continuity and because of its robustness. In our algorithm, the solution variables and their corresponding weight functions are defined as,

$$\overline{p}_h(\boldsymbol{x},t) = \sum_{A\in I_f} p_A(t) N_A(\boldsymbol{x},t), \qquad \overline{w}^1_h(\boldsymbol{x},t) = \sum_{A\in I_f} \overline{w}^1_A(t) N_A(\boldsymbol{x},t), \tag{64}$$

$$\boldsymbol{u}_h(\boldsymbol{X},t) = \sum_{A\in I_s} \boldsymbol{u}_A(t) \widehat{N}_A(\boldsymbol{X}), \qquad \boldsymbol{w}^s_h(\boldsymbol{X}) = \sum_{A\in I_s} \boldsymbol{w}^s_A \widehat{N}_A(\boldsymbol{X}), \tag{65}$$

$$\boldsymbol{u}^m_h(\widetilde{\boldsymbol{x}},\widetilde{t}) = \sum_{A\in I_f} \widehat{\boldsymbol{u}}_A(\widetilde{t}) \widetilde{N}_A(\widetilde{\boldsymbol{x}},\widetilde{t}), \qquad \boldsymbol{w}^m_h(\widetilde{\boldsymbol{x}},\widetilde{t}) = \sum_{A\in I_f} \boldsymbol{w}^m_A \widetilde{N}_A(\widetilde{\boldsymbol{x}},\widetilde{t}), \tag{66}$$

where the coefficients p_A, $\overline{w}^1_A$, $\boldsymbol{u}_A$, $\boldsymbol{w}^s_A$, $\widehat{\boldsymbol{u}}_A$, $\boldsymbol{w}^m_A$ are the control variables, A is a control variable index and $\widehat{N}_A$ is a spline basis function defined on Ω_0. Additionally, I_f and I_s are the index sets of the fluid and solid control variables, respectively. The basis function $N_A(\boldsymbol{x},t)$ is defined as the push forward of $\widehat{N}_A$ to Ω_t, which can be mathematically written as $N_A(\boldsymbol{x},t) = \widehat{N}_A \circ {\boldsymbol{\phi}^h}^{-1}(\boldsymbol{x},t)$ for all $A \in I_f$ while the basis function $\widetilde{N}_A(\widetilde{\boldsymbol{x}},\widetilde{t})$ is the push forward of $\widehat{N}_A$ to the spatial domain at time $\widetilde{t}$, i.e., $\widetilde{N}_A(\widetilde{\boldsymbol{x}},\widetilde{t}) = \widehat{N}_A \circ \widehat{\boldsymbol{\phi}^h}^{-1}(\widetilde{\boldsymbol{x}},\widetilde{t})$ for all $A \in I_f$. We define the $\widehat{N}_A$'s as quadratic splines with $\mathcal{C}^1$-inter-element continuity everywhere except along four parametric lines that enclose the solid domain and include Γ^{sf}_0. The continuity of the $\widehat{N}_A$'s perpendicular to those four parametric lines is $\mathcal{C}^0$. Although our weak form is well defined for $\mathcal{C}^0$ finite elements, we used splines with $\mathcal{C}^1$ interelement continuity everywhere except in the aforementioned four parametric lines because $\mathcal{C}^1$ splines have been shown to have higher accuracy per degree of freedom than $\mathcal{C}^0$ finite elements [65]. The mesh velocity in the spatial configuration is computed as

$$\widehat{\boldsymbol{v}}_h(\boldsymbol{x},t) = \sum_{A\in I_f} \frac{\partial \widehat{\boldsymbol{u}}_A(t)}{\partial t} N_A(\boldsymbol{x},t). \tag{67}$$

The remaining solution variables $(\overline{\boldsymbol{v}}_h, c_{1h}, c_{2h}, \mu_{1h}, \mu_{2h})$ and their corresponding weight functions $(\overline{\boldsymbol{w}}^2_h, w^3_h, w^4_h, w^5_h, w^6_h)$ are defined analogous to $\overline{p}_h(\boldsymbol{x},t)$ and $\overline{w}^1_h(\boldsymbol{x},t)$ in Eq. (64).

3.4. Time integration and solution strategy

We perform time integration of our equations by employing the generalized-α method [66, 67], which has been successfully implemented in phase-field modeling [62] and fluid structure interaction [21, 23, 68].

Let $\boldsymbol{U}$, $\dot{\boldsymbol{U}}$, $\ddot{\boldsymbol{U}}$ be the global vectors of control variables for the fluid-solid system, its first and second time derivatives respectively. Similarly, we denote $\boldsymbol{V}$, $\dot{\boldsymbol{V}}$, $\ddot{\boldsymbol{V}}$ as the global vectors of control variables of mesh displacements, velocities and accelerations respectively. We now define the residual vectors as

$$\boldsymbol{R}^c = \{R^c_A\}, \qquad \boldsymbol{R}^m = \{R^m_{A,i}\}, \qquad \boldsymbol{R}^{c_1} = \{R^{c_1}_A\}, \tag{68}$$

$$\boldsymbol{R}^{c_2} = \{R^{c_2}_A\}, \qquad \boldsymbol{R}^{\mu_1} = \{R^{\mu_1}_A\}, \qquad \boldsymbol{R}^{\mu_2} = \{R^{\mu_2}_A\}, \tag{69}$$

and

$$\boldsymbol{R}^{mesh} = \{R^{mesh}_{A,i}\}, \tag{70}$$

with

$$
\begin{aligned}
R_A^c &= B_{VMS}^f\big((N_A,0,0,0,0,0),(\overline{p}_h,\overline{\boldsymbol{v}}_h,c_{1h},c_{2h},\mu_{1h},\mu_{2h});\hat{\boldsymbol{v}}_h\big),\\
R_{A,i}^m &= B_{VMS}^f\big((0,N_A\boldsymbol{e}_i,0,0,0,0),(\overline{p}_h,\overline{\boldsymbol{v}}_h,c_{1h},c_{2h},\mu_{1h},\mu_{2h});\hat{\boldsymbol{v}}_h\big)\\
&\quad + B^s(\widehat{N}_A\boldsymbol{e}_i,\boldsymbol{u}_h) - T^{sf}\big(N_A\boldsymbol{e}_i,(c_{1h},c_{2h})\big),\\
R_A^{c_1} &= B_{VMS}^f\big((0,0,N_A,0,0,0),(\overline{p}_h,\overline{\boldsymbol{v}}_h,c_{1h},c_{2h},\mu_{1h},\mu_{2h});\hat{\boldsymbol{v}}_h\big),\\
R_A^{c_2} &= B_{VMS}^f\big((0,0,0,N_A,0,0),(\overline{p}_h,\overline{\boldsymbol{v}}_h,c_{1h},c_{2h},\mu_{1h},\mu_{2h});\hat{\boldsymbol{v}}_h\big),\\
R_A^{\mu_1} &= B_{VMS}^f\big((0,0,0,0,N_A,0),(\overline{p}_h,\overline{\boldsymbol{v}}_h,c_{1h},c_{2h},\mu_{1h},\mu_{2h});\hat{\boldsymbol{v}}_h\big),\\
R_A^{\mu_2} &= B_{VMS}^f\big((0,0,0,0,0,N_A),(\overline{p}_h,\overline{\boldsymbol{v}}_h,c_{1h},c_{2h},\mu_{1h},\mu_{2h});\hat{\boldsymbol{v}}_h\big),\\
R_{A,i}^{mesh} &= B^m(\widetilde{N}_A\boldsymbol{e}_i,\boldsymbol{u}_h^m),
\end{aligned}
\tag{71}
$$

where i is the index of the spatial dimension and $\boldsymbol{e}_i$ is the i-th cartesian basis vector. We state our time stepping scheme as follows: find the discrete global vectors of control variables at the time step t_{n+1}, namely, $\boldsymbol{U}_{n+1}$, $\dot{\boldsymbol{U}}_{n+1}$, $\ddot{\boldsymbol{U}}_{n+1}$, $\boldsymbol{V}_{n+1}$, $\dot{\boldsymbol{V}}_{n+1}$, $\ddot{\boldsymbol{V}}_{n+1}$ when $\boldsymbol{U}_n$, $\dot{\boldsymbol{U}}_n$, $\ddot{\boldsymbol{U}}_n$, $\boldsymbol{V}_n$, $\dot{\boldsymbol{V}}_n$, $\ddot{\boldsymbol{V}}_n$ are given at the time step t_n such that

$$
\begin{aligned}
\boldsymbol{R}^c(\boldsymbol{U}_{n+\alpha_f},\dot{\boldsymbol{U}}_{n+\alpha_f},\ddot{\boldsymbol{U}}_{n+\alpha_m},\boldsymbol{V}_{n+\alpha_f},\dot{\boldsymbol{V}}_{n+\alpha_f},\ddot{\boldsymbol{V}}_{n+\alpha_m}) &= 0,\\
\boldsymbol{R}^m(\boldsymbol{U}_{n+\alpha_f},\dot{\boldsymbol{U}}_{n+\alpha_f},\ddot{\boldsymbol{U}}_{n+\alpha_m},\boldsymbol{V}_{n+\alpha_f},\dot{\boldsymbol{V}}_{n+\alpha_f},\ddot{\boldsymbol{V}}_{n+\alpha_m}) &= 0,\\
\boldsymbol{R}^{c_1}(\boldsymbol{U}_{n+\alpha_f},\dot{\boldsymbol{U}}_{n+\alpha_f},\ddot{\boldsymbol{U}}_{n+\alpha_m},\boldsymbol{V}_{n+\alpha_f},\dot{\boldsymbol{V}}_{n+\alpha_f},\ddot{\boldsymbol{V}}_{n+\alpha_m}) &= 0,\\
\boldsymbol{R}^{c_2}(\boldsymbol{U}_{n+\alpha_f},\dot{\boldsymbol{U}}_{n+\alpha_f},\ddot{\boldsymbol{U}}_{n+\alpha_m},\boldsymbol{V}_{n+\alpha_f},\dot{\boldsymbol{V}}_{n+\alpha_f},\ddot{\boldsymbol{V}}_{n+\alpha_m}) &= 0,\\
\boldsymbol{R}^{\mu_1}(\boldsymbol{U}_{n+\alpha_f},\dot{\boldsymbol{U}}_{n+\alpha_f},\ddot{\boldsymbol{U}}_{n+\alpha_m},\boldsymbol{V}_{n+\alpha_f},\dot{\boldsymbol{V}}_{n+\alpha_f},\ddot{\boldsymbol{V}}_{n+\alpha_m}) &= 0,\\
\boldsymbol{R}^{\mu_2}(\boldsymbol{U}_{n+\alpha_f},\dot{\boldsymbol{U}}_{n+\alpha_f},\ddot{\boldsymbol{U}}_{n+\alpha_m},\boldsymbol{V}_{n+\alpha_f},\dot{\boldsymbol{V}}_{n+\alpha_f},\ddot{\boldsymbol{V}}_{n+\alpha_m}) &= 0,\\
\boldsymbol{R}^{mesh}(\boldsymbol{U}_{n+\alpha_f},\dot{\boldsymbol{U}}_{n+\alpha_f},\ddot{\boldsymbol{U}}_{n+\alpha_m},\boldsymbol{V}_{n+\alpha_f},\dot{\boldsymbol{V}}_{n+\alpha_f},\ddot{\boldsymbol{V}}_{n+\alpha_m}) &= 0,
\end{aligned}
\tag{72}
$$

where

$$
\begin{aligned}
(\cdot)_{n+\alpha_f} &= (\cdot)_n + \alpha_f\Big((\cdot)_{n+1} - (\cdot)_n\Big),\\
(\cdot)_{n+\alpha_m} &= (\cdot)_n + \alpha_m\Big((\cdot)_{n+1} - (\cdot)_n\Big),
\end{aligned}
\tag{73}
$$

and

$$
\begin{aligned}
\dot{\boldsymbol{U}}_{n+1} &= \dot{\boldsymbol{U}}_n + \Delta t\left((1-\xi)\ddot{\boldsymbol{U}}_n + \xi\ddot{\boldsymbol{U}}_{n+1}\right),\\
\boldsymbol{U}_{n+1} &= \boldsymbol{U}_n + \Delta t\dot{\boldsymbol{U}}_n + \frac{(\Delta t)^2}{2}\left((1-2\beta)\ddot{\boldsymbol{U}}_n + 2\beta\ddot{\boldsymbol{U}}_{n+1}\right),\\
\dot{\boldsymbol{V}}_{n+1} &= \dot{\boldsymbol{V}}_n + \Delta t\left((1-\xi)\ddot{\boldsymbol{V}}_n + \xi\ddot{\boldsymbol{V}}_{n+1}\right),\\
\boldsymbol{V}_{n+1} &= \boldsymbol{V}_n + \Delta t\dot{\boldsymbol{V}}_n + \frac{(\Delta t)^2}{2}\left((1-2\beta)\ddot{\boldsymbol{V}}_n + 2\beta\ddot{\boldsymbol{V}}_{n+1}\right).
\end{aligned}
\tag{74}
$$

In Eq. (73), $(\cdot)$ denotes the global vector of control variables. To attain second-order accuracy and unconditional stability, we choose the parameters α_f, α_m, ξ and β as per [7, 21].

To solve the discrete formulation of the coupled FSI problem, we adopt a quasi-direct solution strategy; see [21] for more details. We solve the fluid and solid equations in a monolithic fashion,

i.e., fully coupled, while the equations of mesh motion are solved separately using the solution from the former as an input. We solve the nonlinear system of equations given by Eqs. (72) using a Newton-Raphson iterative procedure with a backtracking line search while we solve the linear solver in each Newton iteration using an Algebraic Multigrid with an Additive Schwarz method as a smoother. We check the convergence of the nonlinear solver by ensuring the relative or absolute tolerance of each residual vector in Eq. (72) except $\boldsymbol{R}^{mesh}$ is smaller than 10^{-3} and 10^{-5}, respectively. For $\boldsymbol{R}^{mesh}$, we set the norm of the change in the solution between each Newton step to be 10^{-2}. Because the mesh motion is arbitrary, as long as the boundary conditions are satisfied and the mesh quality is good enough, a larger tolerance for $\boldsymbol{R}^{mesh}$ does not compromise the accuracy of the simulation. Additionally, we set the linear iterative solver to converge until the relative reduction in the preconditioned residual norm is 10^{-5}. Our code was developed using PetIGA [69], an open-source high-performance computing framework employing IGA and built on top of PETSc [70].

4. Numerical examples

In this Section, we present two-dimensional numerical examples of elasto-capillarity with compound droplets using the proposed computational model. We validate our ternary phase field model in our first numerical example. In our subsequent numerical examples, we simulate the static wetting of a compound droplet on a soft solid and the folding of an elastic sheet induced by various types of compound droplets. We neglect the body forces in all our numerical examples, i.e., $\boldsymbol{f} = 0$ and $\boldsymbol{f^s} = 0$.

4.1. Equilibrium shape of a liquid lens

We study a classical example of liquid lens which has been used as a benchmark for validating ternary phase field models. Since this example serves as a validation case for the the fluid mechanics formulation alone, we do not solve the equations of solid dynamics and mesh motion. We initially place three immiscible fluids in contact with each other using the following initial conditions

$$c_2 = \frac{1}{2}\left(1 + \tanh\frac{R_0 - d_0(\boldsymbol{x})}{2\epsilon}\right), \tag{75a}$$

$$c_1 = \max\left(\frac{1}{2}\left(1 + \tanh\frac{y - y_c}{2\epsilon}\right) - c_2, 0\right), \tag{75b}$$

where R_0 is the initial droplet radius and $d_0(\boldsymbol{x})$ is the distance between $\boldsymbol{x}$ and the initial droplet center (x_c, y_c). A fluid lens is attained at equilibrium. The shape of the lens depends on the surface tensions at the three interfaces. The static contact angles (see Fig. 2) at the two triple point junctions at equilibrium satisfy the following relation [42],

$$\frac{\sin\Theta_1}{\gamma_{23}} = \frac{\sin\Theta_2}{\gamma_{13}} = \frac{\sin\Theta_3}{\gamma_{12}}. \tag{76}$$

The static contact angles at equilibrium can also be analytically computed from Neumann's law [42] given by

$$\Theta_i = \cos^{-1}\left(-\frac{\gamma_{ij}^2 + \gamma_{ik}^2 - \gamma_{jk}^2}{2\gamma_{ij}\gamma_{ik}}\right), \ \forall i = 1,2,3, \ i \neq \{j,k\} \text{ and } j \neq k. \tag{77}$$

The analytical distance between the triple point junctions is given by [71]

$$\mathrm{d_{ana}} = 2\sqrt{\frac{\pi R_0^2}{\left(\frac{\pi-\Theta_1}{\sin^2(\pi-\Theta_1)} - \cot(\pi-\Theta_1)\right) + \left(\frac{\pi-\Theta_3}{\sin^2(\pi-\Theta_3)} - \cot(\pi-\Theta_3)\right)}}. \tag{78}$$

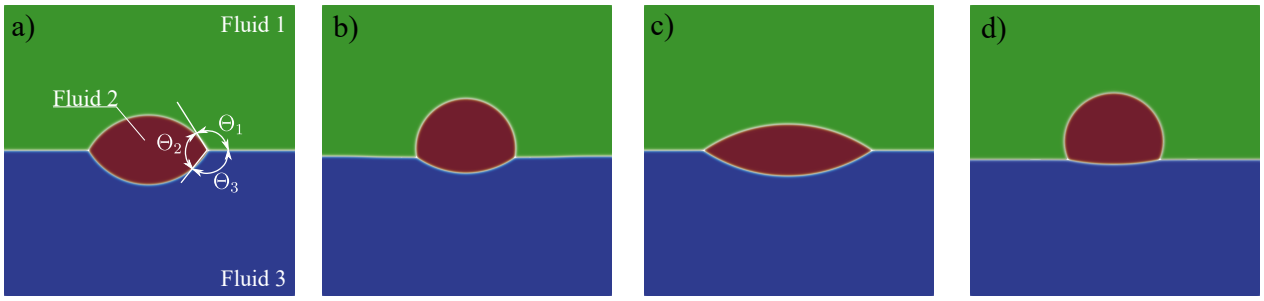

Figure 2: (Color figure online) Equilibrium numerical solutions for different surface tensions: a) $\gamma_{12} = 46.0$ mN/m, $\gamma_{13} = 46.0$ mN/m and $\gamma_{23} = 46.0$ mN/m, b) $\gamma_{12} = 46.0$ mN/m, $\gamma_{13} = 57.5$ mN/m and $\gamma_{23} = 80.5$ mN/m, c) $\gamma_{12} = 46.0$ mN/m, $\gamma_{13} = 77.0$ mN/m and $\gamma_{23} = 46.0$ mN/m, d) $\gamma_{12} = 46.0$ mN/m, $\gamma_{13} = 207.0$ mN/m and $\gamma_{23} = 230.0$ mN/m. The red, blue and green colored regions correspond to $c_2 \geq 0.5, c_3 \geq 0.5$ and $c_1 \geq 0.5$, respectively. We choose a computational domain of size 1000 μm $\times$ 1000 μm and we spatially discretize this domain with a uniform mesh of 256^2 quadratic elements. The initial conditions are defined by a circular drop of fluid 2 with an initial radius $R_0 = 150$ μm at the center $(x_c, y_c) = (500\ \mu\text{m}, 500\ \mu\text{m})$. We impose periodic boundary conditions at the left and right boundaries. At the top and bottom boundaries, we impose no-slip boundary conditions for the velocity, zero diffusive mass flux and neutral wettability. The density and dynamic viscosity of the fluids are equal to those of glycerol, i.e., $\rho = 1260$ kg/m^3 and $\eta = 1.412$ Pa $\cdot$ s. Also, we use $\epsilon = 10$ μm, $M_0 = 10^{-12}$ m^{3}s/kg and $\Delta t = 10.0$ μs.

For the purpose of numerical validation, we simulate four cases with different surface tensions. We show the equilibrium numerical solutions in Fig. 2, which are in excellent agreement with the results previously reported [37, 72]. In Figs. 2a and 2c, the lens is placed symmetrically with respect to fluids 1 and 3. However, in Figs. 2b and 2d, $\gamma_{12} < \gamma_{23}$ and the lens moves closer to fluid 1, which increases the contact area between fluids 1 and 2. We perform a quantitative validation of our results in Fig. 3 by numerically computing the static contact angles and distance between the triple point junctions d_{sim}. For numerical estimation of d_{sim} in Fig. 3, we choose the triple points corresponding to $(c_1, c_2, c_3) = (0.33, 0.33, 0.33)$. As seen in Fig. 3, our numerically computed results are within a relative error of $\pm 3.5\%$ to $\pm 4.0\%$ from the analytical solutions given by Eqs. (77) and (78).

4.2. Static wetting of a compound droplet on soft substrate

When a liquid droplet is placed on a flat and rigid solid, the droplet attains a spherical shape and contacts the solid at an equilibrium contact angle given by Eq. (19). When the solid is sufficiently soft or when the droplet is very small, Eq. (19) breaks down. In that case, the droplet attains an apparent contact angle (with respect to the horizontal), which is different from that given by Eq. (19). The static wetting of a single droplet on a soft solid has been previously studied using experiments [73] and simulations [22, 23, 25]. In [73], the experiments were performed by placing a glycerol droplet on a thin sheet of silicone gel. A wetting ridge was formed when the droplet-air surface tension pulled up the contact line while a dimple was created due to the excess Laplace pressure in the droplet. Here, we study computationally the static wetting of a compound droplet on a soft substrate. Before doing that, and for the sole purpose of validation, we verified that our code and formulation produce quantitatively accurate results when applied to a problem with two fluids only. We accomplished this by taking $c_2 = \gamma_{sf} = 0$ in our model, and verifying that our results (not shown) are identical to those reported in [23, Sec. 4.3].

We now simulate the static wetting of a Janus compound droplet when placed on a soft solid. In the Janus compound droplet configuration, two droplets are in contact with each other; see Fig. 4a. This compound droplet configuration has four triple contact points, i.e., one fluid-fluid-fluid and three fluid-solid-fluid. We consider the fluids in the compound droplet to be water (fluid 1) and oil (fluid 2), both of which are in contact with a surrounding fluid, which we assume to be air (fluid 3). Unless otherwise mentioned, we choose the parameters for this simulation from Table 1 and our time

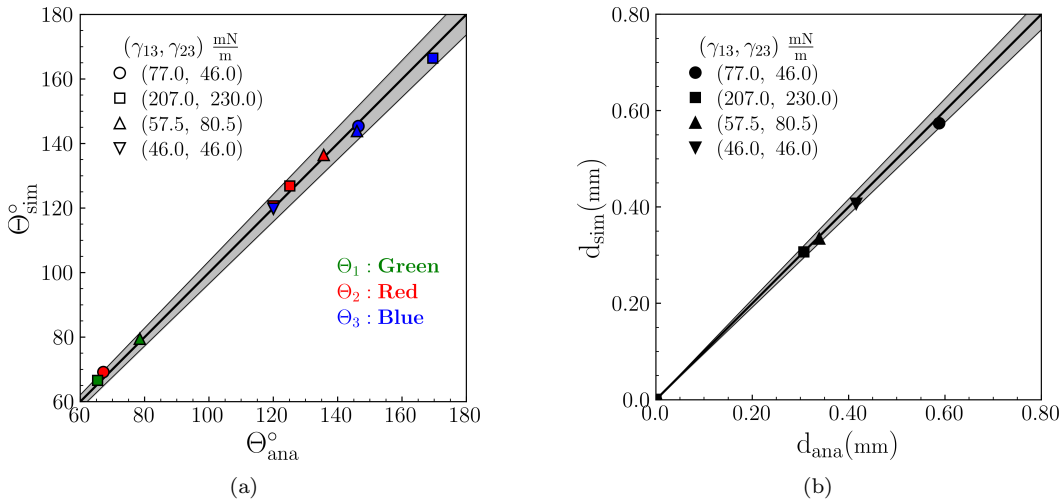

Figure 3: (Color figure online) Comparison of the a) static contact angles and b) distance between the triple point junctions from the present simulation (symbols) and analytical (black solid line) results. We choose $\gamma_{12} = 46.0$ mN/m for all cases. The subscripts sim and ana denote the results from our simulations and analytical expressions, respectively. The gray shaded inset in a) and b) correspond to $\pm 3.5\%$ and $\pm 4\%$ deviation lines from the black solid line, respectively.

step is $\Delta t = 20$ μs. Our model assumes that the three fluids share the same density and dynamic viscosity. We have used the properties of fluid 2, i.e., $\rho = 10^3$ kg/m^3 and $\eta = 1$ Pa $\cdot$ s [74]. The soft substrate is a silicone gel with $E = 3$ kPa [73] and $\rho_0^s = 10^3$ kg/m^3. We use $\gamma_{3s} = 31$ mN/m, which is representative of the surface tension between silicone gel and air [73]. We take $\gamma_{1s} = 50$ mN/m and $\gamma_{2s} = 17$ mN/m. Using Eq. (19), we get $\theta_{13} = 105^\circ, \theta_{23} = 75^\circ$ and $\theta_{12} = 146^\circ$.

We show the schematic of our computational domain, initial conditions and geometrical parameters in the inset of Fig. 4a. Henceforth, we use the notations R_1 and R_2 to denote the initial radii of droplets comprising fluid 1 and fluid 2, respectively. We choose both droplets to have the same volume. We also perform a refinement study by spatially discretizing the computational domain with a uniform mesh of 300×150 (coarse mesh), 400×200 (medium mesh) and 500×250 (fine mesh) quadratic elements. For our refinement study, we fix the ratio of diffuse interface length scale ϵ and the mesh element width to 2. This is because previous research [75] has shown that the diffuse fluid-fluid interface should be thin enough and well resolved to accurately capture the shape and height of the wetting ridge. We choose $\epsilon = 4$ μm, 5 μm and 6.7 μm for the coarse, medium and fine mesh sizes respectively.

Fig. 4a shows our simulations results at $t = 90$ ms (assumed to be the steady state). Fig. 4a also shows that Janus compound droplets produce three wetting ridges at the fluid-solid interface while single-component droplets produce only two. These ridges are areas of significant deformation in the solid due to the action of concentrated forces at the diffuse fluid-fluid interfaces. We show the horizontal and vertical displacements of the solid in Fig. 4b. Fig. 4b shows that the magnitudes of the horizontal and vertical solid displacements are highest around the region where the fluid-fluid interface contacts the solid. We also show the vertical displacement of the fluid-solid interface at the steady state for three different mesh refinement levels in Fig. 5. The depth of the dimple below the water droplet is larger than that below the oil droplet. This is a consequence of the higher Laplace pressure in the water droplet than in the oil droplet.

Symbol	Description	Value
η	Dynamic viscosity of the fluid	$1\ \text{Pa}\cdot\text{s}$
ρ	Fluid density	$10^3\ \text{kg/m}^3$
γ_{13}	Surface tension at the interface between fluids 1 and 3	73 mN/m
γ_{23}	Surface tension at the interface between fluids 2 and 3	55 mN/m
γ_{12}	Surface tension at the interface between fluids 1 and 2	40 mN/m
γ_{1s}	Surface tension at the interface between the solid and fluid 1	12 mN/m
γ_{2s}	Surface tension at the interface between the solid and fluid 2	45 mN/m
γ_{3s}	Surface tension at the interface between the solid and fluid 3	31 mN/m
M_0	Mobility coefficient	$10^{-14}\ \text{m}^3\text{s/kg}$
ν	Poisson's ratio	0.45
ρ_0^s	Mass density of solid in the referential configuration	$10^3\ \text{kg/m}^3$

Table 1: Parameter values employed for the elasto-capillary simulations.

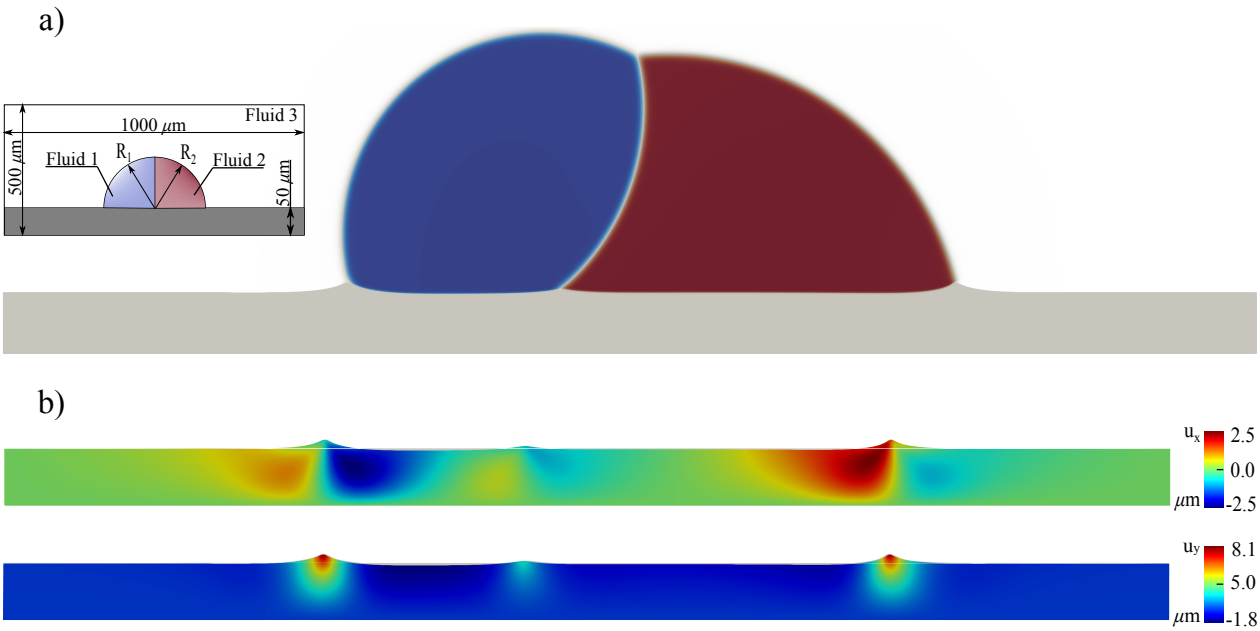

Figure 4: (Color figure online) Static wetting of a Janus compound droplet on a soft solid. a) Steady state configuration showing how the compound droplet deforms the solid. The inset shows the schematic of the computational domain, initial conditions and geometrical parameters in the simulations. The figure in the inset is not drawn to scale. b) Horizontal and vertical displacements of the solid, respectively. We initially place the droplets at $(500.0\ \mu\text{m}, 50.0\ \mu\text{m})$. We impose zero velocity in the normal directions at the left, right and top boundaries of the domain. At the bottom boundary, we impose zero velocity in both the normal and tangential directions. We choose $R_1 = 225.5\ \mu$m and $R_2 = 225.5\ \mu$m. Blue and red colored droplets denote water and oil, respectively.

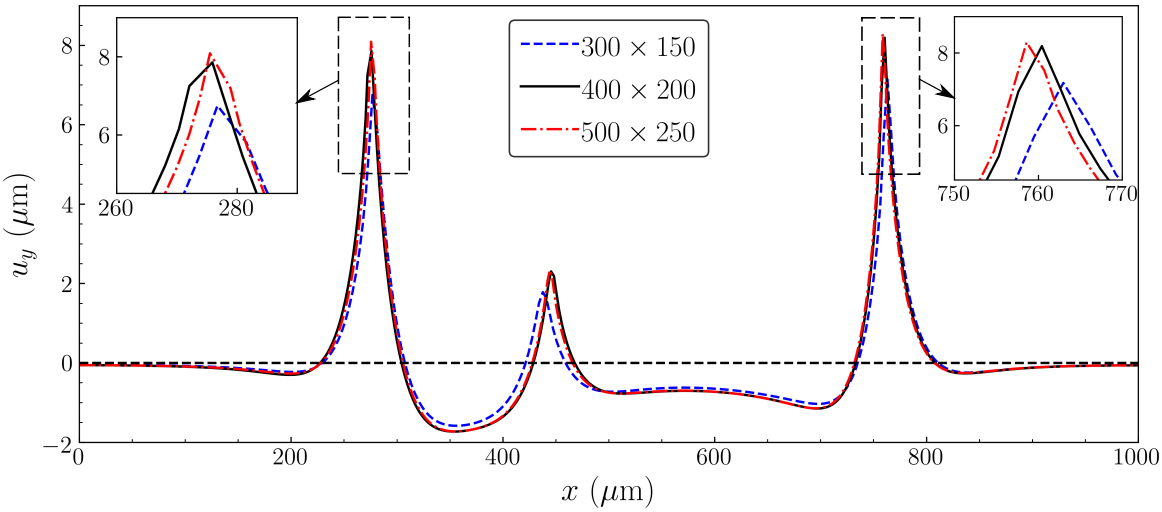

Figure 5: (Color figure online) Vertical displacement of the fluid-solid interface u_y along the horizontal direction at $t = 90$ ms (assumed to be the steady state) for three different mesh refinement levels. The zoomed insets show views of the wetting ridges. The horizontal dashed line in black represents the fluid-solid interface before solid deformation.

4.3. Capillary origami of compound droplets

The spontaneous wrapping of a droplet with an elastic sheet driven by capillary forces has been termed capillary origami and studied experimentally [4]. The experiments in [4] were performed by placing a thin elastic sheet on top of a rigid surface. Then, a liquid droplet was deposited on the thin elastic sheet, which led to the folding of the elastic sheet. Modeling this problem in its entirety would require a contact algorithm. Another challenge is that the fluid domain undergoes a topological change. Thus, we simplify the problem by ignoring the underlying rigid solid surface and neglecting gravity forces. Here, we focus on the capillary folding of a flexible sheet when in contact with a compound droplet. We consider the fluids in the compound droplets to be water (fluid 1) and oil (fluid 2), both of which are in contact with a surrounding fluid, which we assume to be air (fluid 3).

Unless otherwise mentioned, we choose the parameters for our simulations from Table 1 and our time step is $\Delta t = 20$ μs. The flexible sheet is a soft hydrogel with $E = 30$ kPa [76, 77] and $\rho_0^s = 10^3$ kg/m^3. Unless otherwise mentioned, we assume the sheet to be hydrophilic-oleophobic, i.e., water attracting and oil repelling. On hydrophilic and hydrophobic surfaces, water droplet attains static contact angles of less than 90° and more than 90°, respectively. The combined hydrophilicity and oleophobicity of a surface can be controlled either with a fluorosurfactant [78] or by spray coating [79]. To enforce the combined hydrophilicity and oleophobicity of the sheet, we fix $\gamma_{1s} = 12$ mN/m and $\gamma_{2s} = 45$ mN/m. Using Eq. (19), we get $\theta_{13} = 75°, \theta_{23} = 105°$ and $\theta_{12} = 34°$. We show the schematic of our computational domain, initial conditions and geometrical parameters in Fig. 6. Fig. 6 shows the four different types of compound droplets that we study, namely, Janus, collar, lens and encapsulated. These four types represent the most common compound droplet configurations. The initial geometry of the solid is identical in all examples. We spatially discretize the computational domain with a uniform mesh of 400 × 200 quadratic elements.

4.3.1. Janus compound droplets

In the Janus compound droplet configuration, two droplets are in contact with each other; see Fig. 6a. This compound droplet configuration has four triple contact points, i.e., one fluid-fluid-fluid and three fluid-solid-fluid. In our simulation, both droplets have the same volume. We show

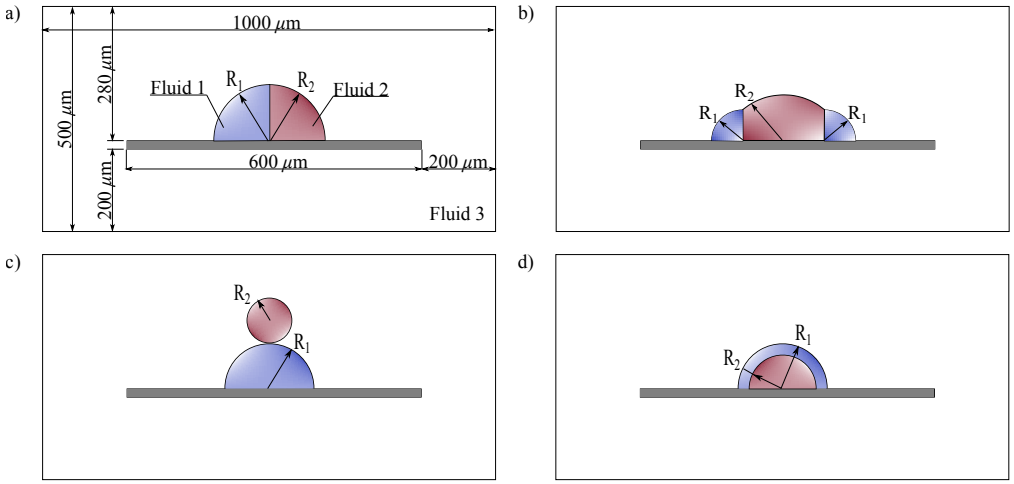

Figure 6: (Color figure online) Schematic of the computational domain, initial conditions and geometrical parameters in the simulations involving a) Janus, b) collar, c) lens and d) encapsulated droplet configurations. Figures are not drawn to scale.

the temporal evolution of the Janus droplet and sheet in Fig. 7. Our focus is on the effects of surface wettability on the folding of the sheet. As shown in Fig. 7, we simulate three cases with different surface wettabilities. In Case I, we enforce all solid-fluid surface tensions to be equal, i.e., $\gamma_{1s} = \gamma_{2s} = \gamma_{3s} = 31$ mN/m. In Case II, we assume a higher surface wettability of the sheet with oil by using $\gamma_{1s} = 50$ mN/m and $\gamma_{2s} = 17$ mN/m. In Case III, we assume a higher surface wettability of the sheet with water by using $\gamma_{1s} = 12$ mN/m and $\gamma_{2s} = 45$ mN/m. The initial positions and initial volumes of each droplet are the same for all cases. In all cases, we observe progressive folding of the elastic sheet as time advances. Although the initial condition is symmetric, the folding develops in a non-symmetric way, even for Case I in which all solid-fluid surface tensions are equal. In Case I, the symmetry is broken because the fluid-fluid surface tensions γ_{12} and γ_{23} are different. The symmetry breaking is a particular feature of capillary origami of compound droplets that does not easily occur with two fluids only. The presence of the third wetting ridge at an intermediate point between the left and right contact lines seems to hinder the folding process.

We show the temporal evolution of the folding angles for Cases I and III in Fig. 8. The folding angle is defined as per the schematic in Fig. 8a. A smaller folding angle signifies an easier folding of the sheet. We observe that the folding of the sheet is determined by the effects of the surface tension of the fluid with air and the surface wettability of the sheet with the fluid. The sheet gets better folded if the surface tension of the fluid with air or the surface wettability of the sheet with the fluid is high. In Case I, the surface wettabilities of the sheet with water and oil are the same. But the surface tension of water with air is higher than that of oil with air, and this explains why water better folds the sheet than oil in Case I; see Fig. 8a. In addition to the large surface tension of water with air, the surface wettability of the sheet with water is higher than that of the sheet with oil in Case III. That is why, water better folds the sheet than oil in this case as well; see Fig. 8c.

Figs. 7 and 8 show that both the surface wettability and fluid-fluid surface tensions play a crucial role in folding the sheet. This may be important in applications involving self-assembly of micro- and nano-structures.

4.3.2. Collar compound droplets

In the collar compound droplet configuration, a central droplet is surrounded by two droplets on either sides. The droplets on the sides are comprised of the same fluid, which is different from

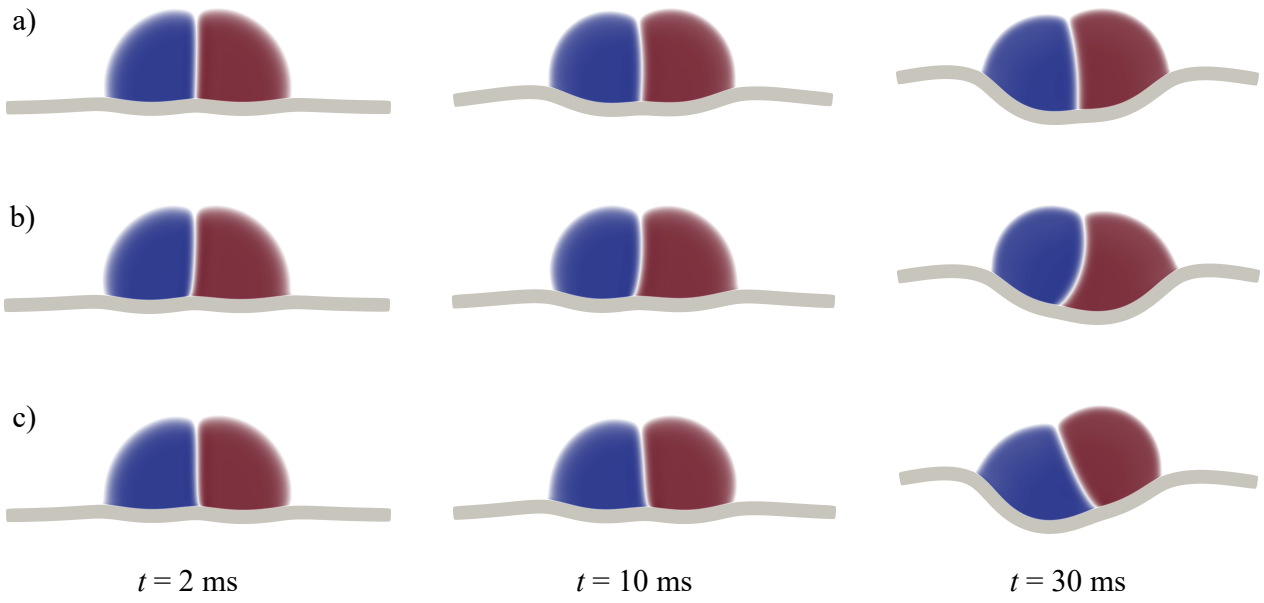

Figure 7: (Color figure online) Capillary origami of Janus compound droplets for a) Case I: $\gamma_{1s} = 31$ mN/m, $\gamma_{2s} = 31$ mN/m and $\gamma_{3s} = 31$ mN/m, b) Case II: $\gamma_{1s} = 50$ mN/m, $\gamma_{2s} = 17$ mN/m and $\gamma_{3s} = 31$ mN/m, c) Case III: $\gamma_{1s} = 12$ mN/m, $\gamma_{2s} = 45$ mN/m and $\gamma_{3s} = 31$ mN/m. These cases correspond to a) $\theta_{13} = 90^\circ$ and $\theta_{23} = 90^\circ$, b) $\theta_{13} = 105^\circ$ and $\theta_{23} = 75^\circ$ and c) $\theta_{13} = 75^\circ$ and $\theta_{23} = 105^\circ$. We choose $R_1 = 145$ μm, $R_2 = 145$ μm and $\epsilon = 15$ μm. The droplets are initially placed at $(500.0\ \mu\text{m}, 220.0\ \mu\text{m})$. Blue and red colored droplets denote water and oil, respectively.

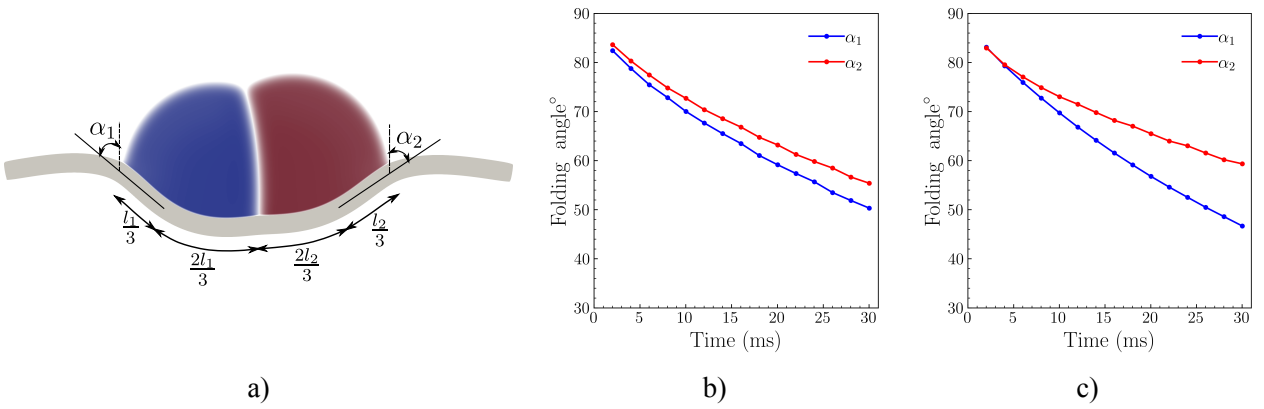

Figure 8: (Color figure online) a) Definition of the folding angles α_1 (for fluid 1) and α_2 (for fluid 2). For fluid 1, the angle is defined with respect to the average slope of the solid sheet in on third of the solid length wetted by fluid 1. An analogous definition applies to fluid 2. b) and c) Temporal variation of the folding angles in Janus compound droplets for Case I and Case III, respectively.

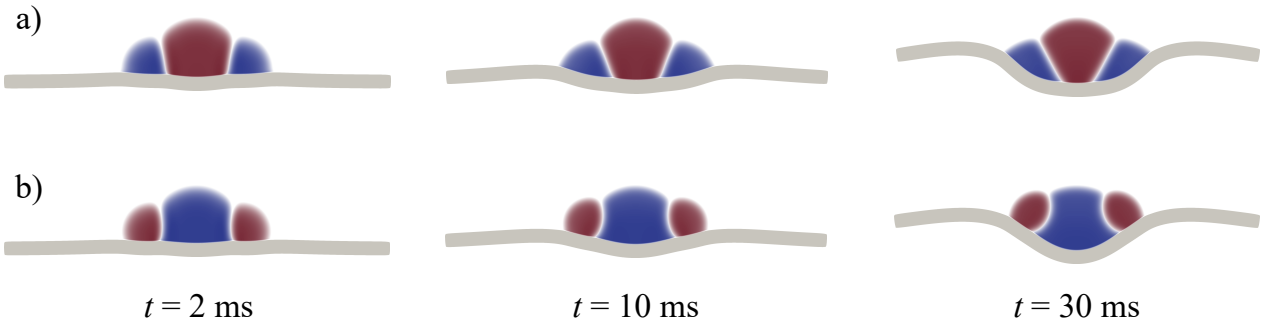

Figure 9: (Color Figure online) Capillary origami of collar compound droplets. We choose $\epsilon = 15$ μm, a) $R_1 = 60$ μm and $R_2 = 80$ μm, b) $R_1 = 80$ μm and $R_2 = 60$ μm, respectively. In both cases, the droplets are initially placed at $(413.4\ \mu\text{m}, 220.0\ \mu\text{m}), (500.0\ \mu\text{m}, 220.0\ \mu\text{m})$ and $(586.6\ \mu\text{m}, 220.0\ \mu\text{m})$. Blue and red colored droplets denote water and oil, respectively.

that of the central droplet; see Fig. 6b. This compound droplet configuration has six triple contact points, i.e., two fluid-fluid-fluid and four fluid-solid-fluid. This leads to the formation of four ridges in the solid. We perform two simulations. In the first one (Fig. 9a), the side droplets are comprised of fluid 1, while in the second one (Fig. 9b), the side droplets are comprised of fluid 2. In our simulations, the droplets on either sides of the central droplet have the same volume. The droplet configuration in Fig. 9b better folds the sheet than in Fig. 9a because of the higher volume of water droplet which is in contact with the sheet. In [80], the authors demonstrate the capillary folding of a sheet in the presence of only one droplet. They also study the dependence of the folding angle at equilibrium on the droplet volume. The authors report the folding angle to decrease with an increase in the droplet volume. Our observation on the dependence of the folding angle with the water droplet's volume also shows that the droplet volumes play a crucial role in folding the sheet.

4.3.3. Lens compound droplets

In the lens compound droplet configuration, a fluid droplet is placed over another fluid droplet; see Fig. 6c. We show the temporal evolution of the droplet and sheet in Fig. 10 when water is placed over oil and vice-versa. This compound droplet configuration initially has three triple contact points, i.e., two fluid-solid-fluid and one fluid-fluid-fluid; see Fig. 6. As the compound droplet evolves with time, it attains four triple contact points, i.e., two fluid-solid-fluid and two fluid-fluid-fluid; see Fig. 10. We observe a better folding of the sheet when oil is placed over water (Fig. 10a) than when water is placed over oil (Fig. 10b). This is due to the higher surface wettability of the sheet with water than oil. In [23], the authors simulate the capillary folding of a sheet in the case of a single droplet only. They observed a faster folding of the sheet when using a wetting droplet than when using a non-wetting droplet. This implies that, at the same time instant, the authors should observe a better folding of the sheet when the surface wettability of the sheet with the fluid is high. Using theoretical calculations, the authors in [80] also report a better folding of the sheet when the sheet is hydrophilic in contrast to a hydrophobic sheet. Our conclusions from Fig. 10 on the dependence of the folding angle with the surface wettability of the sheet match the observations in [23] and [80].

4.3.4. Encapsulated compound droplets

In the encapsulated compound droplet configuration, a fluid encloses another immiscible fluid; see Fig. 6d. This compound droplet configuration has four triple contact points. We show the temporal evolution of the droplet and sheet in Fig. 11. In Fig. 11a, we observe that the length of solid wetted by oil decreases with time. The limited contact of oil with the sheet at $t = 20$ ms is

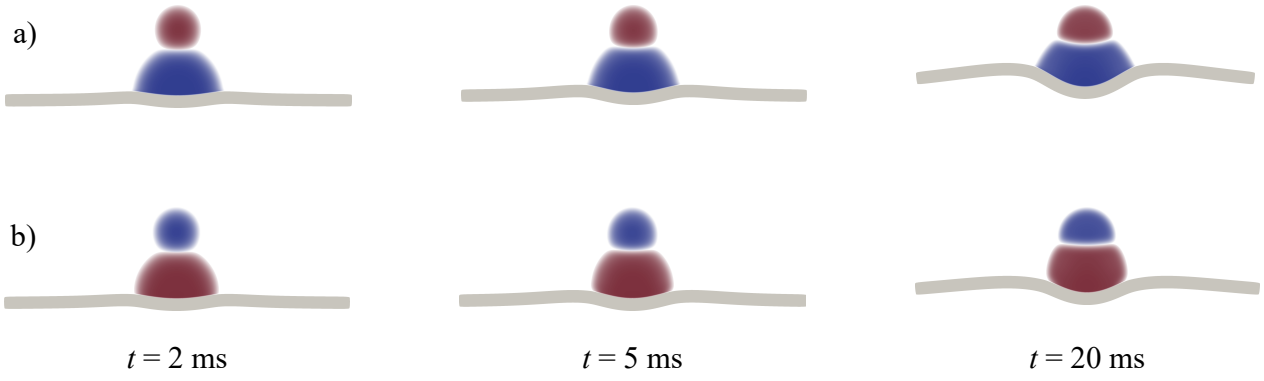

Figure 10: (Color figure online) Capillary origami of lens compound droplets. We choose $\epsilon = 15$ μm, a) $R_1 = 75.0$ μm and $R_2 = 37.5$ μm, b) $R_1 = 37.5$ μm and $R_2 = 75.0$ μm, respectively. The droplets are initially placed at a) $(500.0\ \mu\text{m}, 220.0\ \mu\text{m})$ and $(500.0\ \mu\text{m}, 332.5\ \mu\text{m})$, b) $(500.0\ \mu\text{m}, 332.5\ \mu\text{m})$ and $(500.0\ \mu\text{m}, 220.0\ \mu\text{m})$, respectively. Blue and red colored droplets denote water and oil, respectively.

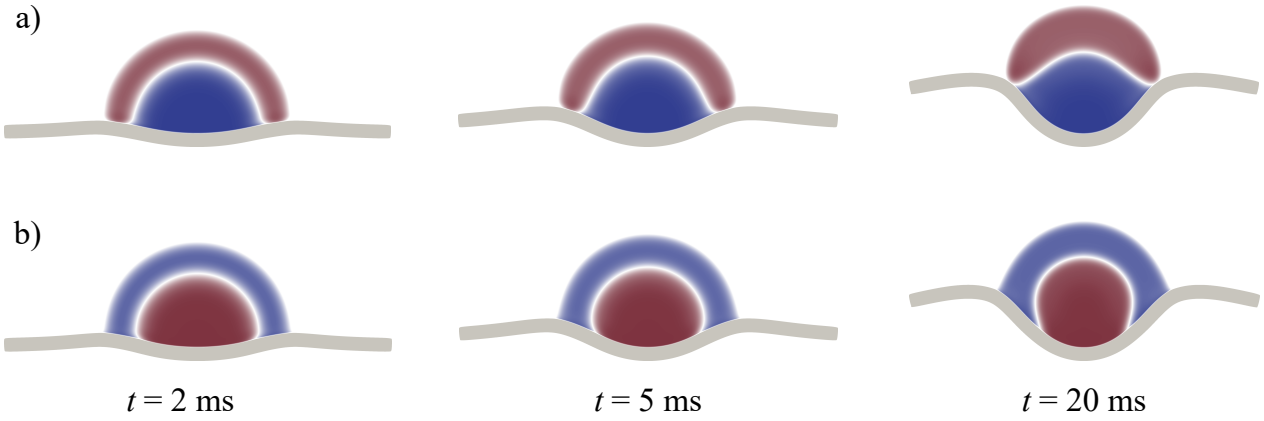

Figure 11: (Color figure online) Capillary origami of encapsulated compound droplets. We choose $\epsilon = 15$ μm, a) $R_1 = 100$ μm and $R_2 = 145$ μm, b) $R_1 = 145$ μm and $R_2 = 100$ μm, respectively. In both cases, the droplets are initially placed at $(500.0\ \mu\text{m}, 220.0\ \mu\text{m})$ and $(500.0\ \mu\text{m}, 220.0\ \mu\text{m})$. Blue and red colored droplets denote water and oil, respectively.

due to the large surface tension at the solid-oil interface. Comparing Figs. 11a and 11b, we see that the sheet is better folded when water is enclosed in oil. This is because the volume of the water droplet which is in contact with the sheet is higher in Fig. 11a than in 11b.

For a given set of physical parameters like volumes of the droplet or surface tensions, recent work [81] has reported a dynamic transition in the compound droplet configuration. Understanding this transition is of pivotal importance in industrial applications where generation or reconfiguration of compound droplets is also possible by simply changing these physical parameters [82, 83]. For example, encapsulated compound droplets are used in drug delivery applications [84]. In these applications, a transition in the compound droplet configuration could possibly lead to an escape of the enclosed fluid, which could prove fatal. Here, we simulate an example to show this dynamic transition in the compound droplet configuration; see Fig. 12. For this example, we choose oil with a higher surface tension at the interface with air and water such that $\gamma_{23} = 84$ mN/m and $\gamma_{12} = 42$ mN/m. We also change the surface tension at the water-solid and oil-solid interfaces, i.e., $\gamma_{1s} = 18$ mN/m and $\gamma_{2s} = 50$ mN/m. These values yield static contact angles of $\theta_{13} = 80^\circ$ and $\theta_{12} = 40^\circ$ from Eq. (19). We start with an initially encapsulated droplet configuration where water encloses oil. With the passage of time, we notice a transition to a collar droplet configuration at

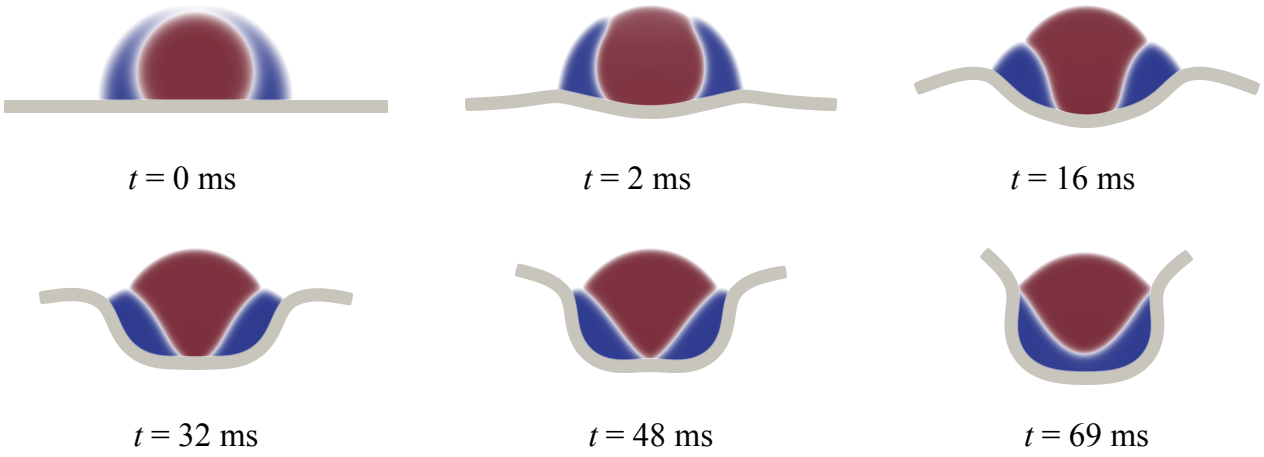

Figure 12: (Color figure online) Dynamical transition in the compound droplet configuration from encapsulated-collar-encapsulated type. We choose $\epsilon = 15$ μm, $R_1 = 145$ μm and $R_2 = 94$ μm. The droplets are initially placed at (500.0 μm, 220.0 μm) and (500.0 μm, 262.0 μm). We select the physical parameters with $\gamma_{12} = 42$ mN/m, $\gamma_{13} = 73$ mN/m, $\gamma_{23} = 84$ mN/m, $\gamma_{1s} = 18$ mN/m, $\gamma_{2s} = 50$ mN/m and $\gamma_{3s} = 31$ mN/m. These chosen values yield $\theta_{13} = 80^\circ$ and $\theta_{12} = 40^\circ$.

$t = 2$ ms. Due to the higher surface wettability of the sheet with water than with oil, the water droplets eventually merge at $t = 48$ ms. Later, the droplet configuration transits from a collar at $t = 48$ ms to an encapsulated droplet configuration at $t = 69$ ms, with oil now enclosing water. This example suggests a potential way of controlling the compound droplet configuration by simply varying the surface wettabilities or droplet volumes.

We show the temporal evolution of the streamlines of the fluid velocity in Fig. 13. The streamlines are symmetrical with respect to the vertical axis due to our assumptions in geometry. The dynamic folding of the sheet results in a pair of counter-rotating vortices at the base of the droplets and near the walls of the computational domain. The fluid velocity inside the central droplets at $t = 16$ and 32 ms is mainly vertically oriented without the presence of any vortices. The streamlines at $t = 69$ ms show a notable exception, due to two pairs of counter-rotating vortices inside the central droplet. The inset in Fig. 13c shows a close-up view of the solid and fluid meshes. The solid mesh was not distorted during the motion. However, the fluid mesh has undergone significant deformation. The image shows that 20 layers of fluid elements adjacent to the fluid-solid interface are less distorted. This is because we used a stiffer material for the fictitious elastic problem that defines mesh motion, which helped us to avoid excessive element distortion that would have led to singular mapping.

In all, this example illustrates the complexity of elasto-capillary folding with compound droplets and highlights the need for high-fidelity computational models.

5. Conclusions

We have presented a mathematical model and algorithm for simulation of elasto-capillary FSI problems involving three immiscible fluids, for example, in compound droplets. We have employed a phase-field model given by the ternary NSCH equations and a neo-Hookean model for the solid. Our motivation for choosing the phase-field model is because it avoids contact-line stress singularities, describes the dynamic wetting behavior, captures moving contact lines and enforces thermodynamical consistency of the model. We have leveraged a fluid-solid surface energy function, which controls the fluid-solid wettability and determines the tractions transmitted to the solid at the fluid-solid interface. We have additionally enforced consistency conditions like in [37] to derive the surface

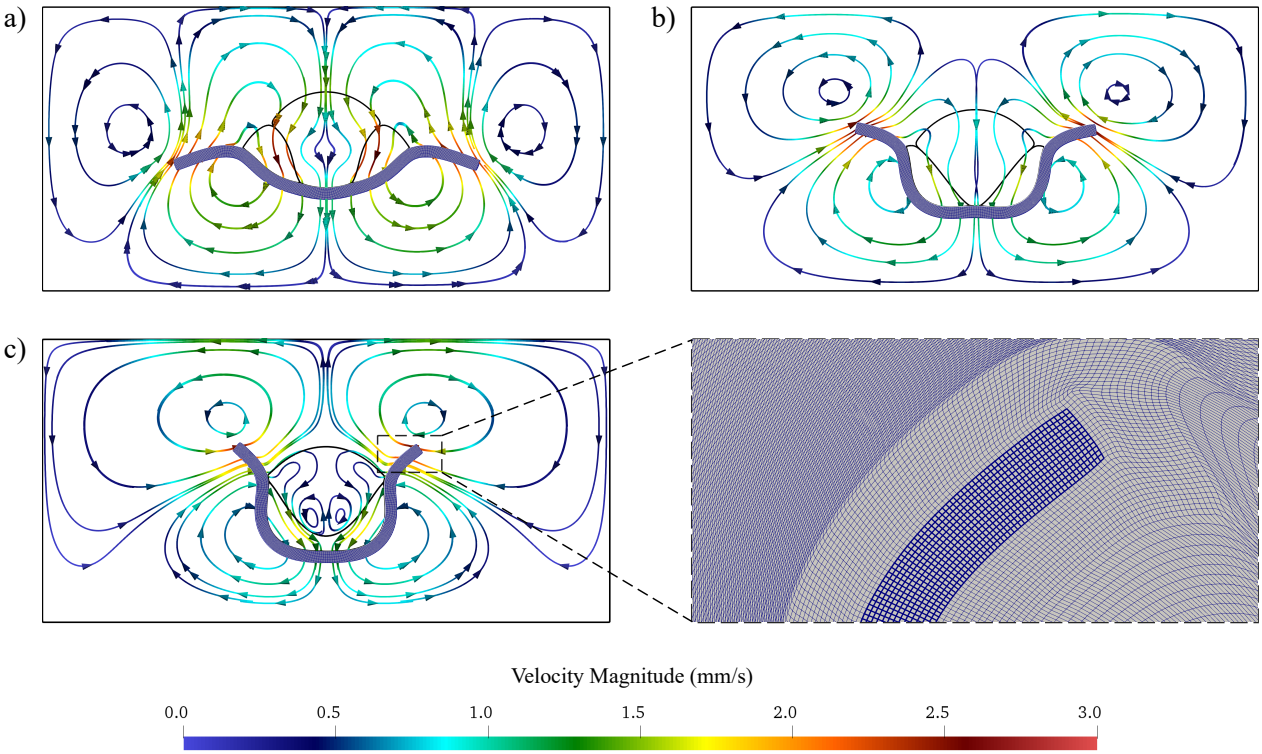

Figure 13: (Color figure online) Solid mesh and streamlines of the fluid velocity during the dynamical transition of the compound droplet from an encapsulated configuration at a) $t = 16$ ms, b) $t = 32$ ms and c) $t = 69$ ms. The arrows indicate the direction of the fluid velocity. The streamlines and the arrows are colored by the magnitude of the fluid velocity. Fluid-fluid interfaces are represented by black solid lines. The zoomed inset in c) shows a small region of the computational mesh at $t = 69$ ms.

energy function and wettability boundary conditions. We have performed spatial discretization using IGA and employed generalized-α method for time integrating the semi-discrete equations. We have also adopted a boundary-fitted approach for our FSI formulation because this approach can accurately compute the capillary forces at the fluid-solid interface.

Using our computational model, we have successfully simulated the static wetting of Janus compound droplet on a soft solid and the elasto-capillary folding of a thin elastic solid under the action of different types of compound droplets (Janus, collar, lens and encapsulated). In our static wetting simulations, we observed the magnitudes of the horizontal and vertical solid displacements to be highest where the droplet contacts the solid. In our simulations of capillary origami, we observed the presence of more than two wetting ridges in Janus, encapsulated and collar droplets, a phenomenon that is unique to compound droplets. These ridges appeared between the left and right contact lines, and hindered the folding of the sheet. The folding of the sheet was observed to depend on the surface wettability of the sheet, fluid-fluid surface tensions and droplet volumes. We have also simulated a dynamic transition in the compound droplet configuration from an encapsulated to a collar type. Achieving this transition was possible by changing the relative volumes of the fluid, surface wettability or the fluid-fluid surface tensions. Our numerical examples reveal the complexity of elasto-capillarity involving compound droplets, which motivates the need for high-fidelity computational models.

This work opens a number of new opportunities for future research. From a fundamental perspective, our computational model can be used to understand migration of compound droplets on deformable solids; see [85] for a recent work on migration of encapsulated compound droplets in pressure-driven channel flows. Our model may also assist in understanding collective cell migration on soft solids driven by heterotypic interactions, i.e., interactions between different cell types [86]. From a modeling perspective, our model, theory and algorithm can be extended to include the effects of droplet evaporation; see [87] for a recent development of two-phase two-component phase-field theory. Such models will help us better understand evaporative-driven microfabrication or evaporative-driven transition in the compound droplet configurations [35].

Declaration of Competing Interest

The authors declare that they have no known competing financial interests or personal relationships that could have appeared to influence the work reported in this paper.

Acknowledgements

This research was partially supported by the National Science Foundation (Award no. CBET 2012242). SRB thanks Adrian Moure for the discussions regarding the open-source PetIGA framework and Yu Leng for proofreading the manuscript.

Appendix A. Derivation of Eq. (35)

Listing 1: This MATLAB code computes the left-hand side of Eq. (35) and stores it in `hfunction`.

```
syms gamma_1s gamma_2s gamma_3s gamma_12 gamma_13 gamma_23
syms c c1 c2 c3 g12 g13 g23 G G12 G13 G23
sigma_1 = gamma_12 + gamma_13 - gamma_23;
sigma_2 = gamma_12 + gamma_23 - gamma_13;
sigma_3 = gamma_13 + gamma_23 - gamma_13;
R = gamma_1s*(3*c1^2 - 2*c1^3) + gamma_2s*(3*c2^2 - 2*c2^3) + gamma_3s*(3*c3^2 - 2*c3^3);
g12 = c1*c2/(1 - c1)/(1 - c2);
g13 = c1*c3/(1 - c1)/(1 - c3);
g23 = c3*c2/(1 - c3)/(1 - c2);
G12 = (gamma_1s*sigma_2 + gamma_2s*sigma_1)/gamma_12;
```

```
G23 = (gamma_2s*sigma_3 + gamma_3s*sigma_2)/gamma_23;
G13 = (gamma_1s*sigma_3 + gamma_3s*sigma_1)/gamma_13;
G = (3*G12*g12 + 3*G13*g13 + 3*G23*g23);
gammasf_drv_c1 = diff(simplify(R + c1*c2*c3*G), c1);
gammasf_drv_c2 = diff(simplify(R + c1*c2*c3*G), c2);
gammasf_drv_c3 = diff(simplify(R + c1*c2*c3*G), c3);
delta = 6/(1/sigma_1 + 1/sigma_2 + 1/sigma_3);
h = -(delta/6)*(gammasf_drv_c1/sigma_1 + gammasf_drv_c2/sigma_2 + gammasf_drv_c3/sigma_3);
hfunction = simplify(subs(h, {c1, c3, c2}, {c, 0, 1-c}))
```

References

[1] C. C. Long, A. L. Marsden, Y. Bazilevs, Fluid–structure interaction simulation of pulsatile ventricular assist devices, Computational Mechanics 52 (5) (2013) 971–981.

[2] J. Yan, A. Korobenko, X. Deng, Y. Bazilevs, Computational free-surface fluid–structure interaction with application to floating offshore wind turbines, Computers & Fluids 141 (2016) 155–174.

[3] V. Anand, I. C. Christov, Transient compressible flow in a compliant viscoelastic tube, Physics of Fluids 32 (11) (2020) 112014.

[4] C. Py, P. Reverdy, L. Doppler, J. Bico, B. Roman, C. N. Baroud, Capillary Origami: Spontaneous Wrapping of a Droplet with an Elastic Sheet, Physical Review Letters 98 (15) (2007) 156103.

[5] J. Huang, M. Juszkiewicz, W. H. De Jeu, E. Cerda, T. Emrick, N. Menon, T. P. Russell, Capillary wrinkling of floating thin polymer films, Science 317 (5838) (2007) 650–653.

[6] E. H. Dowell, K. C. Hall, Modeling of fluid-structure interaction, Annual Review of Fluid Mechanics 33 (1) (2001) 445–490.

[7] Y. Bazilevs, V. M. Calo, T. J. R. Hughes, Y. Zhang, Isogeometric fluid-structure interaction: theory, algorithms, and computations, Computational Mechanics 43 (1) (2008) 3–37.

[8] G. Hou, J. Wang, A. Layton, Numerical Methods for Fluid-Structure Interaction — a review, Communications in Computational Physics 12 (2) (2012) 337–377.

[9] A. Soria, F. Casadei, Arbitrary Lagrangian–Eulerian multicomponent compressible flow with fluid–structure interaction, International Journal for Numerical Methods in Fluids 25 (11) (1997) 1263–1284.

[10] X. Zheng, G. E. Karniadakis, A phase-field/ALE method for simulating fluid–structure interactions in two-phase flow, Computer Methods in Applied Mechanics and Engineering 309 (2016) 19–40.

[11] V. Joshi, R. K. Jaiman, A hybrid variational Allen-Cahn/ALE scheme for the coupled analysis of two-phase fluid-structure interaction, International Journal for Numerical Methods in Engineering 117 (4) (2019) 405–429.

[12] M. Vahab, M. Sussman, K. Shoele, Fluid-structure interaction of thin flexible bodies in multi-material multi-phase systems, Journal of Computational Physics 429 (2021) 110008.

[13] K. Yan, J. Li, L. Pan, Y. Shi, Inkjet printing for flexible and wearable electronics, APL Materials 8 (12) (2020) 120705.

[14] M. Srinivasarao, D. Collings, A. Philips, S. Patel, Three-Dimensionally Ordered Array of Air Bubbles in a Polymer Film, Science 292 (5514) (2001) 79–83.

[15] M. L. Manning, R. A. Foty, M. S. Steinberg, E.-M. Schoetz, Coaction of intercellular adhesion and cortical tension specifies tissue surface tension, Proceedings of the National Academy of Sciences 107 (28) (2010) 12517–12522.

[16] R. W. Style, Y. Che, S. J. Park, B. M. Weon, J. H. Je, C. Hyland, G. K. German, M. P. Power, L. A. Wilen, J. S. Wettlaufer, E. R. Dufresne, Patterning droplets with durotaxis, Proceedings of the National Academy of Sciences 110 (31) (2013) 12541–12544.

[17] J. Bueno, Y. Bazilevs, R. Juanes, H. Gomez, Wettability control of droplet durotaxis, Soft Matter 14 (8) (2018) 1417–1426.

[18] J. Bueno, Y. Bazilevs, R. Juanes, H. Gomez, Droplet motion driven by tensotaxis, Extreme Mechanics Letters 13 (2017) 10–16.

[19] A. T. Bradley, F. Box, I. J. Hewitt, D. Vella, Wettability-Independent Droplet Transport by *Bendotaxis*, Physical Review Letters 122 (7) (2019) 074503.

[20] E. Cerda, L. Mahadevan, Geometry and physics of wrinkling, Physical Review Letters 90 (7) (2003) 074302.

[21] J. Bueno, C. Bona-Casas, Y. Bazilevs, H. Gomez, Interaction of complex fluids and solids: theory, algorithms and application to phase-change-driven implosion, Computational Mechanics 55 (6) (2015) 1105–1118.

[22] E. H. van Brummelen, M. S. Roudbari, G. Şimşek, K. G. van der Zee, Binary-fluid–solid interaction based on the Navier–Stokes–Cahn–Hilliard Equations, De Gruyter, 2017, pp. 283–328.

[23] J. Bueno, H. Casquero, Y. Bazilevs, H. Gomez, Three-dimensional dynamic simulation of elastocapillarity, Meccanica 53 (6) (2018) 1221–1237.

[24] M. Shokrpour Roudbari, E. Van Brummelen, Binary-fluid–solid interaction based on the Navier–Stokes–Korteweg equations, Mathematical Models and Methods in Applied Sciences 29 (05) (2019) 995–1036.

[25] S. Aland, P. Auerbach, A ternary phase-field model for wetting of soft elastic structures, International Journal for Numerical Methods in Engineering 122 (16) (2021) 4114–4128.

[26] S. Aland, D. Mokbel, A unified numerical model for wetting of soft substrates, International Journal for Numerical Methods in Engineering 122 (4) (2021) 903–918.

[27] M. Pepona, A. Shek, C. Semprebon, T. Krüger, H. Kusumaatmaja, Modeling ternary fluids in contact with elastic membranes, Physical Review E 103 (2) (2021) 022112.

[28] H. Gomez, M. Velay-Lizancos, Thin-film model of droplet durotaxis, The European Physical Journal Special Topics 229 (2) (2020) 265–273.

[29] H. Gomez, K. G. van der Zee, Computational Phase-Field Modeling, Encyclopedia of Computational Mechanics (second Edition), 978-1-119-00379-3, John Wiley & Sons, Ltd., 2017, pp. 1–35.

[30] D. Jacqmin, Contact-line dynamics of a diffuse fluid interface, Journal of Fluid Mechanics 402 (2000) 57–88.

[31] P.-G. De Gennes, F. Brochard-Wyart, D. Quéré, Capillarity and Wetting Phenomena: Drops, Bubbles, Pearls, Waves, Vol. 315, Springer, 2004.

[32] P.-G. De Gennes, Wetting: statics and dynamics, Reviews of Modern Physics 57 (3) (1985) 827.

[33] P. Yue, J. J. Feng, Wall energy relaxation in the Cahn-Hilliard model for moving contact lines, Physics of Fluids 23 (1) (2011) 012106.

[34] E. H. van Brummelen, M. Shokrpour-Roudbari, G. Van Zwieten, Elasto-capillarity simulations based on the Navier–Stokes–Cahn–Hilliard Equations, in: Advances in Computational Fluid-Structure Interaction and Flow Simulation, Springer, 2016, pp. 451–462.

[35] M. J. Neeson, R. F. Tabor, F. Grieser, R. R. Dagastine, D. Y. Chan, Compound sessile drops, Soft Matter 8 (43) (2012) 11042–11050.

[36] N. Blanken, M. S. Saleem, M.-J. Thoraval, C. Antonini, Impact of compound drops: a perspective, Current Opinion in Colloid & Interface Science 51 (2021) 101389.

[37] F. Boyer, C. Lapuerta, Study of a three component Cahn-Hilliard flow model, ESAIM: Mathematical Modelling and Numerical Analysis-Modélisation Mathématique et Analyse Numérique 40 (4) (2006) 653–687.

[38] Y. Bazilevs, K. Takizawa, T. E. Tezduyar, Computational fluid-structure interaction: methods and applications, John Wiley & Sons, 2013.

[39] J. A. Cottrell, T. J. R. Hughes, Y. Bazilevs, Isogeometric Analysis: Toward Integration of CAD and FEA, John Wiley & Sons, 2009.

[40] T. J. R. Hughes, J. A. Cottrell, Y. Bazilevs, Isogeometric analysis: CAD, finite elements, NURBS, exact geometry and mesh refinement, Computer Methods in Applied Mechanics and Engineering 194 (39-41) (2005) 4135–4195.

[41] F. Boyer, C. Lapuerta, S. Minjeaud, B. Piar, M. Quintard, Cahn–Hilliard/Navier–Stokes Model for the Simulation of Three-Phase Flows, Transport in Porous Media 82 (3) (2010) 463–483.

[42] J. S. Rowlinson, B. Widom, Molecular Theory of Capillarity, Courier Corporation, 2013.

[43] N. Bala, M. Pepona, I. Karlin, H. Kusumaatmaja, C. Semprebon, Wetting boundaries for a ternary high-density-ratio lattice Boltzmann method, Physical Review E 100 (1) (2019) 013308.

[44] C.-Y. Zhang, H. Ding, P. Gao, Y.-L. Wu, Diffuse interface simulation of ternary fluids in contact with solid, Journal of Computational Physics 309 (2016) 37–51.

[45] S. Dong, Wall-bounded multiphase flows of N immiscible incompressible fluids: Consistency and contact-angle boundary condition, Journal of Computational Physics 338 (2017) 21–67.

[46] R. Shuttleworth, The Surface Tension of Solids, Proceedings of the Physical Society. Section A 63 (5) (1950) 444.

[47] Q. Zhang, X.-P. Wang, Phase field modeling and simulation of three-phase flow on solid surfaces, Journal of Computational Physics 319 (2016) 79–107.

[48] J. C. Simo, T. J. R. Hughes, Computational Inelasticity, Vol. 7, Springer New York, 1998.

[49] S. Gross, A. Reusken, Numerical Methods for Two-phase Incompressible Flows, Vol. 40, Springer, 2011.

[50] G. C. Buscaglia, R. F. Ausas, Variational formulations for surface tension, capillarity and wetting, Computer Methods in Applied Mechanics and Engineering 200 (45-46) (2011) 3011–3025.

[51] J. C. Slattery, L. Sagis, E.-S. Oh, Interfacial transport phenomena, Springer New York, 2007.

[52] T. Wick, Fluid-structure interactions using different mesh motion techniques, Computers & Structures 89 (13-14) (2011) 1456–1467.

[53] J. Donea, A. Huerta, J.-P. Ponthot, A. Rodríguez-Ferran, Arbitrary Lagrangian–Eulerian Methods, Vol. 3, Encyclopedia of Computational Mechanics, Fluids, 2004, Ch. 14.

[54] T. Hu, Y. Leng, H. Gomez, A novel method to impose boundary conditions for higher-order partial differential equations, Computer Methods in Applied Mechanics and Engineering 391 (2022) 114526.

[55] Y. Leng, T. Hu, S. R. Bhopalam, H. Gomez, Numerical solutions of a gradient-elastic Kirchhoff plate model on convex and concave geometries using isogeometric analysis, Journal of Mechanics 38 (2022) 238–249.

[56] T. J. R. Hughes, G. Scovazzi, L. P. Franca, Multiscale and stabilized methods, Encyclopedia of Computational Mechanics Second Edition, Wiley Online Library, 2017, pp. 1–64.

[57] A. N. Brooks, T. J. R. Hughes, Streamline upwind/Petrov-Galerkin formulations for convection dominated flows with particular emphasis on the incompressible Navier-Stokes equations, Computer Methods in Applied Mechanics and Engineering 32 (1-3) (1982) 199–259.

[58] T. Tezduyar, S. Sathe, Stabilization Parameters in SUPG and PSPG Formulations, Journal of Computational and Applied Mechanics 4 (1) (2003) 71–88.

[59] J. U. Brackbill, D. B. Kothe, C. Zemach, A continuum method for modeling surface tension, Journal of Computational Physics 100 (2) (1992) 335–354.

[60] Y. Bazilevs, V. Calo, J. Cottrell, T. J. R. Hughes, A. Reali, G. Scovazzi, Variational multiscale residual-based turbulence modeling for large eddy simulation of incompressible flows, Computer Methods in Applied Mechanics and Engineering 197 (1) (2007) 173–201.

[61] T. J. R. Hughes, G. Sangalli, Variational Multiscale Analysis: the Fine-scale Green's Function, Projection, Optimization, Localization, and Stabilized Methods, SIAM Journal on Numerical Analysis 45 (2) (2007) 539–557.

[62] H. Gómez, V. M. Calo, Y. Bazilevs, T. J. R. Hughes, Isogeometric analysis of the Cahn–Hilliard phase-field model, Computer Methods in Applied Mechanics and Engineering 197 (49) (2008) 4333 – 4352.

[63] H. Gomez, T. J. R. Hughes, X. Nogueira, V. M. Calo, Isogeometric analysis of the isothermal Navier–Stokes–Korteweg equations, Computer Methods in Applied Mechanics and Engineering 199 (25-28) (2010) 1828–1840.

[64] B. S. Hosseini, S. Turek, M. Möller, C. Palmes, Isogeometric Analysis of the Navier–Stokes–Cahn–Hilliard equations with application to incompressible two-phase flows, Journal of Computational Physics 348 (2017) 171–194.

[65] T. J. Hughes, A. Reali, G. Sangalli, Duality and unified analysis of discrete approximations in structural dynamics and wave propagation: comparison of p-method finite elements with k-method nurbs, Computer methods in applied mechanics and engineering 197 (49-50) (2008) 4104–4124.

[66] K. E. Jansen, C. H. Whiting, G. M. Hulbert, A generalized-α method for integrating the filtered Navier–Stokes equations with a stabilized finite element method, Computer methods in applied mechanics and engineering 190 (3-4) (2000) 305–319.

[67] J. Chung, G. M. Hulbert, A Time Integration Algorithm for Structural Dynamics With Improved Numerical Dissipation: The Generalized-α Method, Journal of Applied Mechanics 60 (2) (1993) 371–375.

[68] H. Casquero, C. Bona-Casas, H. Gomez, A NURBS-based immersed methodology for fluid–structure interaction, Computer Methods in Applied Mechanics and Engineering 284 (2015) 943–970.

[69] L. Dalcin, N. Collier, P. Vignal, A. Côrtes, V. Calo, PetIGA: A framework for high-performance isogeometric analysis, Computer Methods in Applied Mechanics and Engineering 308 (2016) 151 – 181.

[70] S. Balay, S. Abhyankar, M. F. Adams, J. Brown, P. Brune, K. Buschelman, L. Dalcin, A. Dener, V. Eijkhout, W. D. Gropp, D. Karpeyev, D. Kaushik, M. G. Knepley, D. A. May, L. C. McInnes, R. T. Mills, T. Munson, K. Rupp, P. Sanan, B. F. Smith, S. Zampini, H. Zhang, H. Zhang, PETSc Web page, https://www.mcs.anl.gov/petsc (2019).

[71] Y. Hu, D. Li, Q. He, Generalized conservative phase field model and its lattice Boltzmann scheme for multicomponent multiphase flows, International Journal of Multiphase Flow 132 (2020) 103432.

[72] R. H. H. Abadi, M. H. Rahimian, A. Fakhari, Conservative phase-field lattice-Boltzmann model for ternary fluids, Journal of Computational Physics 374 (2018) 668–691.

[73] R. W. Style, R. Boltyanskiy, Y. Che, J. S. Wettlaufer, L. A. Wilen, E. R. Dufresne, Universal Deformation of Soft Substrates Near a Contact Line and the Direct Measurement of Solid Surface Stresses, Physical Review Letters 110 (2013) 066103.

[74] Pubchem compound summary for cid 14030006, castor oil, https://pubchem.ncbi.nlm.nih.gov/compound/Castor-oil, accessed: 2022-04-07.

[75] B. Hosseini, Isogeometric analysis of cahn–hilliard phase field–based binary–fluid–structure interaction based on an ALE variational formulation, Ph.D. thesis, TU Dortmund, https://eldorado.tu-dortmund.de/handle/2003/40171(Aug. 2020).

[76] M. V. Flores-Merino, S. Chirasatitsin, C. LoPresti, G. C. Reilly, G. Battaglia, A. J. Engler, Nanoscopic mechanical anisotropy in hydrogel surfaces, Soft Matter 6 (18) (2010) 4466–4470.

[77] J. Bae, T. Ouchi, R. C. Hayward, Measuring the Elastic Modulus of Thin Polymer Sheets by Elasto-capillary Bending, ACS Applied Materials & Interfaces 7 (27) (2015) 14734–14742.

[78] P. S. Brown, B. Bhushan, Bioinspired, roughness-induced, water and oil super-philic and super-phobic coatings prepared by adaptable layer-by-layer technique, Scientific Reports 5 (1) (2015) 1–16.

[79] J. Yang, Z. Zhang, X. Xu, X. Zhu, X. Men, X. Zhou, Superhydrophilic–superoleophobic coatings, Journal of Materials Chemistry 22 (7) (2012) 2834–2837.

[80] J.-P. Péraud, E. Lauga, Geometry and wetting of capillary folding, Physical Review E 89 (4) (2014) 043011.

[81] C.-Y. Zhang, P. Gao, E.-Q. Li, H. Ding, On the compound sessile drops: configuration boundaries and transitions, Journal of Fluid Mechanics 917 (2021) A37.

[82] L. Mahadevan, M. Adda-Bedia, Y. Pomeau, Four-phase merging in sessile compound drops, Journal of Fluid Mechanics 451 (2002) 411–420.

[83] R. Iqbal, S. Dhiman, A. K. Sen, A. Q. Shen, Dynamics of a Water Droplet over a Sessile Oil Droplet: Compound Droplets Satisfying a Neumann Condition, Langmuir 33 (23) (2017) 5713–5723.

[84] D.-H. Lee, Y.-M. Goh, J.-S. Kim, H.-K. Kim, H.-H. Kang, K.-D. Suh, J.-W. Kim, Effective Formation of Silicone-in-Fluorocarbon-in-Water Double Emulsions: Studies on Droplet Morphology and Stability, Journal of dispersion science and technology 23 (4) (2002) 491–497.

[85] A. Tiribocchi, A. Montessori, M. Lauricella, F. Bonaccorso, S. Succi, S. Aime, M. Milani, D. A. Weitz, The vortex-driven dynamics of droplets within droplets, Nature Communications 12 (1) (2021) 1–10.

[86] A. K. Mishra, J. P. Campanale, J. A. Mondo, D. J. Montell, Cell interactions in collective cell migration, Development 146 (23) (2019) 172056.

[87] S. Mukherjee, H. Gomez, Flow and mixing dynamics of phase-transforming multicomponent fluids, Applied Physics Letters 115 (10) (2019) 104101.